

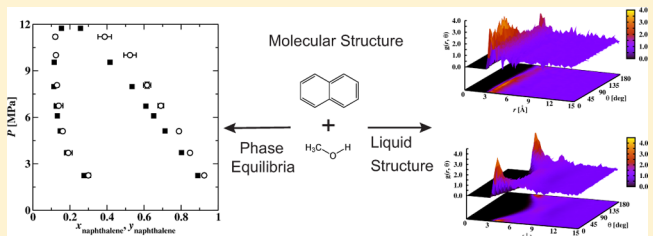
Transferable Potentials for Phase Equilibria. 10. Explicit-Hydrogen Description of Substituted Benzenes and Polycyclic Aromatic Compounds

Neeraj Rai and J. Ilja Siepmann*

Department of Chemistry, Department of Chemical Engineering and Materials, and Chemical Theory Center, University of Minnesota, 207 Pleasant Street SE, Minneapolis, Minnesota 55455, United States

Supporting Information

ABSTRACT: The explicit-hydrogen version of the transferable potentials for phase equilibria (TraPPE-EH) force field is extended to various substituted benzenes through the parametrization of the exocyclic groups —F, —Cl, —Br, —C≡N, and —OH and to polycyclic aromatic hydrocarbons through the parametrization of the aromatic linker carbon atom for multiple rings. The linker carbon together with the TraPPE-EH parameters for aromatic heterocycles constitutes a force field for fused-ring heterocycles. Configurational-bias Monte Carlo simulations in the Gibbs ensemble were carried out to compute vapor–liquid coexistence curves for fluorobenzene; chlorobenzene; bromobenzene; di-, tri-, and hexachlorobenzene isomers; 2-chlorofuran; 2-chlorothiophene; benzonitrile; phenol; dihydroxybenzene isomers; 1,4-benzoquinone; naphthalene; naphthalene-2-carbonitrile; naphthalen-2-ol; quinoline; benzo[b]-thiophene; benzo[c]-thiophene; benzoxazole; benzisoxazole; benzimidazole; benzothiazole; indole; isoindole; indazole; purine; anthracene; and phenanthrene. The agreement with the limited experimental data is very satisfactory, with saturated liquid densities and vapor pressures reproduced to within 1.5% and 15%, respectively. The mean unsigned percentage errors in the normal boiling points, critical temperatures, and critical densities are 0.9%, 1.2%, and 1.4%, respectively. Additional simulations were carried out for binary systems of benzene/benzonitrile, benzene/phenol, and naphthalene/methanol to illustrate the transferability of the developed potentials to binary systems containing compounds of different polarity and hydrogen-bonding ability. A detailed analysis of the liquid-phase structures is provided for selected neat systems and binary mixtures.



1. INTRODUCTION

Aromatic molecules or subunits are present in many biological assemblies, pharmaceutical compounds, manufactured polymers, and organic semiconductor materials. More than two-thirds of all known organic chemicals are either aromatic or contain aromatic subunits, and nearly half of them are heterocycles.^{1,2} The special nonbonded interactions, often referred to as π – π interactions, and the planarity exhibited by aromatic compounds play a key role in numerous biochemical processes (such as neurotransmission), drug–DNA binding, supramolecular and polymer chemistry, and crystal engineering applications.^{1–13}

The relatively “weak” intermolecular interactions occurring in aromatic compounds present significant challenges for the quantitative determination of these interactions through experiments^{14–16} and electronic structure calculations.^{17–26} Molecular simulations provide a complementary approach for determining effective intermolecular potentials, or force fields. Substantial improvements in the simulation algorithms (and, to a lesser extent, in computational speed) now allow for very precise predictions of the thermophysical properties of organic compounds with molecular weights up to about 500 au. Hence, these simulations can be used to assess the accuracy of the force field used to describe a given compound and, in turn, to

develop more accurate force fields. In many cases, the force field parameters for Lennard-Jones potentials (or similar repulsive–dispersive potentials) and, sometimes, the partial atomic charges (describing the first-order electrostatic interactions) are obtained by fitting to experimental data, such as the liquid density and heat of vaporization.

All of the popular force fields developed for the simulation of biological systems provide the interaction parameters for the most common substituted aromatics and aromatic heterocycles.^{27–34} However, the accuracy of these force fields often deteriorates at elevated temperatures and pressures and is not satisfactory for predictions of fluid-phase equilibria because their parametrization process is usually limited to condensed-phase data at ambient conditions. The anisotropic united atom (AUA) force field is aimed at the prediction of thermophysical properties over a wide range of state conditions and provides parameters for a number of simple aromatic compounds, such as benzene, naphthalene, polycyclic aromatic hydrocarbons, alkylbenzenes, and thiophene, but currently lacks parameters for other heterocyclic aromatic and substituted aromatic

Received: July 24, 2012

Revised: October 28, 2012

Published: December 3, 2012

compounds.^{35–41} Hence, a force field that can accurately reproduce the thermophysical properties for large set of aromatic molecules over a wide range of physical conditions is much needed.

An ongoing effort of this research group has been the development of the transferable potentials for phase equilibria (TraPPE) force field that is simple yet accurate and transferable. The TraPPE force field parameters are mostly fitted using the vapor–liquid equilibrium (VLE) data of selected compounds (usually, the smallest members of a homologous series), but binary VLE data and triple-point data are also used in some cases.^{42,43} The TraPPE force field is available for alkanes (linear and branched);^{44–46} alkenes;^{47,48} alcohols;⁴⁹ ethers;⁵⁰ aldehydes;⁵⁰ ketones;⁵⁰ amines;⁵¹ amides;⁵¹ nitroalkanes;⁵¹ sulfides;⁵² disulfides;⁵² thiols;⁵² benzene;^{43,53} aromatic heterocycles;⁴³ acrylates;⁴⁸ phosphonates;⁵⁴ and small molecules such as water,⁵⁵ carbon dioxide,⁴² ethylene oxide,⁵⁶ nitrogen,⁴² and ammonia.⁵⁷ For alkanes, benzene, nitrobenzene, pyridine, pyrimidine, and thiophene, the TraPPE force field provides a choice of using either the united-atom (UA) or the explicit-hydrogen (EH) representation of CH_x groups. The UA version of the force field is simple and results in considerable savings of computer time, whereas the EH version usually provides more accurate saturated vapor pressures and heats of vaporization at a higher computational cost. Previous work has shown that an explicit description of benzene's quadrupole moment is essential to accurately describe its solid–fluid phase behavior^{58,59} and its mixtures with aliphatic hydrocarbons.⁵³ The UA version for aromatic heterocycles and substituted aromatics uses partial charges only on the polar heteroatoms/functional groups and the α carbons. In contrast, the corresponding EH models distribute partial charges over all atomic sites to better account for the diffusiveness of the electron density in aromatic molecules. These partial charges are computed for each specific aromatic molecule using an electronic structure calculation in a continuum solvent.⁴³

In two previous publications, the TraPPE-EH models for benzene and five- and six-membered aromatic compounds containing N, O, and S heteroatoms⁴³ (please note that there is a typographical mistake in ref 43 and the correct partial charges for benzene are $q_{\text{C}} = -q_{\text{H}} = -0.095|\text{el}|$) and for aniline, nitrobenzene, and 1,3,5-triamino-2,4,6-trinitrobenzene⁶⁰ were introduced. In the present work, the TraPPE-EH force field is extended to fluorobenzene, (mono-, di-, tri, and hexa-) chlorobenzene isomers, bromobenzene, benzonitrile, benzoquinone, phenol, dihydroxybenzene isomers, naphthalene, quinoline, benzo[b]thiophene, benzo[c]thiophene, benzoxazole, benzisoxazole, benzimidazole, benzothiazole, indole, isoindole, indazole, and purine. The remainder of this article is organized as follows: The force field and parametrization philosophy are described in section 2, and the simulation details are provided in section 3. In section 4, the vapor–liquid coexistence curves (VLCCs) for the molecules used in the parametrization are presented. As an assessment of the transferability of the force field, VLCCs are predicted for additional molecules and some binary systems. Furthermore, some of the structural features of these systems are discussed.

2. FORCE FIELD DEVELOPMENT

The TraPPE force field uses standard Lennard-Jones (LJ) and Coulomb potentials to describe nonbonded interactions

$$U(r_{ij}) = 4\epsilon_{ij} \left[\left(\frac{\sigma_{ij}}{r_{ij}} \right)^{12} - \left(\frac{\sigma_{ij}}{r_{ij}} \right)^6 \right] + \frac{q_i q_j}{4\pi\epsilon_0 r_{ij}} \quad (1)$$

where r_{ij} , σ_{ij} , ϵ_{ij} , q_i , q_j , and ϵ_0 are the distance between a pair of interacting sites i and j , the LJ diameter, the LJ well depth, the partial charges on interaction sites i and j , and the permittivity of a vacuum, respectively. The LJ parameters used in this work are listed in Table 1, and the partial atomic charges for each

Table 1. TraPPE-EH Lennard-Jones Parameters for Substituted Benzenes and Fused-Ring Aromatic Heterocycles^a

atom type	ref	ϵ/k_{B} (K)	σ (Å)
X(aro)—C(aro)—X(aro)	43	30.70	3.60
H—C(aro)	43	25.45	2.36
H—N/O(aro)	43	12.00	0.50
C(aro)—N(aro)—X(aro)	43	57.00	3.20
C(aro)—O(aro)—X(aro)	43	70.00	2.60
C(aro)—S(aro)—X(aro)	43	158.00	3.55
F—C(aro)	this work	27.50	2.85
Cl—C(aro)	this work	149.00	3.42
Br—C(aro)	this work	210.00	3.60
O phenol	this work	118.00	3.04
N nitrile(aro)	this work	60.00	2.95
C nitrile(aro)	this work	20.00	3.38
O=C(aro) 1,4-benzoquinone	this work	90.00	2.95
O=C(aro) 1,4-benzoquinone	this work	30.00	3.45
C fused-ring link atom	this work	55.00	3.20

^aBold and regular fonts indicate the specific atom and its bonding environment, respectively. X(aro) indicates a neighboring atom that is either C(aro), N(aro), O(aro), or S(aro).

molecule are provided in the Supporting Information. The Lorentz–Berthelot (LB)^{61,62} combining rules are used to determine LJ parameters for unlike interaction sites in the TraPPE-EH force field. This choice is made for two reasons: (a) The LB combining rules are already implemented in most simulation packages and, hence, afford ease of use, and (b) the TraPPE parametrization strategy implicitly compensates for some deficiencies of the LB combining rules. It is well-known that the LB combining rules work best for sites with similar LJ diameters (e.g., atoms in the same row of the periodic table),⁶³ whereas problems arise for sites with rather different LJ diameters.^{64–66} The LJ diameters for the heavy atoms used in this work range from 2.60 to 3.60 Å, whereas those for the nonpolar and polar hydrogen atoms are considerably smaller. However, the bead-by-bead parametrization strategy (starting from the benzene molecule) used here requires that new LJ parameters for heteroatoms work in conjunction with the existing hydrogen parameters where unlike interactions are determined by the LB combining rules.

The TraPPE-EH force field treats aromatic rings and the directly connected exocyclic atoms as rigid entities, and hence, there are no intramolecular interactions. The intramolecular structures of all aromatic compounds were determined from geometry optimization at the B3P86/6-311+G(3df,3pd) level of theory^{67,68} and basis set.⁶⁹ A computer-readable file with the structural information is provided in the Supporting Information. A previous investigation for benzene showed that allowing for bond bending and dihedral flexibility has only a negligible effect on its VLCC and solid–vapor phase equilibria.⁷⁰

However, if flexibility is desired for algorithmic reasons, then harmonic force constants from other force fields can be used in combination with the bond lengths and bending angles used for the TraPPE-EH force field that can be deduced from the molecular structures provided in the Supporting Information.

Similarly to aniline and nitrobenzene,⁶⁰ phenol and the dihydroxybenzene isomers are treated as semiflexible, that is, the C(aro)—O—H bending motion and the dihedral rotation around the C(aro)—O bond are governed by a harmonic angle bending potential and a cosine series dihedral potential, respectively, whereas the O—H bond length is fixed. For semiflexible molecules with multiple substituents, the intramolecular geometry is adjusted to reflect the symmetry of the core. For example, the formation of an intramolecular H-bond in the geometry-optimized structure of 1,2-dihydroxybenzene would otherwise lead to different C(aro)—O bond lengths and different C(aro)—C(aro)—O and C(aro)—O—H bond angles for the two hydroxyl groups. To reproduce the correct energetic gain for the formation of the intramolecular H-bond in the 1,2-dihydroxybenzene structure, different dihedral potentials are used for the C(O)—C—O—H and C(H)—C—O—H dihedral angles. Details of the intramolecular bending and dihedral potentials for phenol and the dihydroxybenzene isomers are provided in the Supporting Information.

The methodology used in the development of the TraPPE force field is to minimize the number of different parameters required to model a homologous series of a particular functional group, hence ensuring the ability to build larger molecules that contain this functional group. In the present work, the same parametrization philosophy is used to determine the LJ diameters and well depths, and only the LJ parameters for the substituent groups are fitted to experimental data for selected compounds, whereas the LJ parameters for the carbon ring atom connected to the substituent group are taken without change from the TraPPE-EH benzene model.⁴³

Because the charge density of aromatic compounds is much more diffuse and delocalized in comparison to that of aliphatic hydrocarbons, the effect of substituent polar groups or heteroatoms is not confined to only the neighboring α carbon atoms, but affects the charge density of the entire aromatic ring(s). This results in nontransferability of the partial charges used to represent the electron density. The atom-centered partial charges for the aromatic molecules are obtained using the CM4 charge model.⁷¹ To reflect the polarization effects present in condensed phases, the CM4 charges are determined in a continuum solvation environment,⁷¹ where the TraPPE-EH parametrization employs 1-octanol as its universal continuum solvent because it provides a good balance of polar and nonpolar character. To determine the partial atomic charges, the gas-phase optimized geometries are used in the self-consistent continuum solvation calculations employing the same Kohn–Sham density functionals as for the geometry optimization but with the smaller 6-31+G** basis set. The MN-GSM version 6 module was used for these calculations.⁷²

Once the partial atomic charges for a given molecule are assigned, LJ parameters are fitted to the saturated liquid density and the vapor pressure over a wide range of temperatures. Starting from the LJ parameters for benzene and heteroatoms in the five-membered and six-membered aromatic rings, new parameters were developed for the following substituent atoms (all connected to the ring by a single bond): F, Cl, Br, C and N (for the nitrile group), and O (for the hydroxyl group where

the LJ parameters for the polar hydrogen are taken from the TraPPE-EH for aromatic heterocycles⁴³). Because of the double-bond character of the substituent present in *p*-benzoquinone, the LJ parameters for both of the atoms involved in the C=O group are fitted here. The LJ parameters for F, Cl, Br, and O (in the hydroxyl group) are obtained by carrying out simulations for neat fluorobenzene, chlorobenzene, bromobenzene, and phenol, respectively. For the nitrile group, the LJ parameters for carbon and nitrogen atoms are simultaneously fit to saturated liquid densities and vapor pressures of neat benzonitrile. The lack of experimental VLCC data for *p*-benzoquinone led us to use crystal structure data to refine the LJ parameters obtained from fitting to its normal boiling point. The LJ parameters for the carbon linker atom for the fused-ring aromatic compounds are parametrized to data for neat naphthalene.

3. SIMULATION DETAILS

3.1. Single-Component VLCCs. Gibbs-ensemble Monte Carlo (GEMC) simulations^{73,74} were carried out to compute the VLCCs for pure compounds. The system consisted of 250 molecules. A spherical cutoff (r_{cut}) of 14 Å was used for the LJ potential, together with analytical tail corrections⁷⁵ to account for the LJ interaction energy beyond the cutoff. The Ewald summation with tin foil boundary conditions^{75,76} was employed to compute the electrostatic interactions. The cutoff used for the real-space part of the Ewald summation was set to r_{cut} , and the Ewald sum convergence parameter, κ , was set to $3.2/r_{\text{cut}}$. For the reciprocal-space part of the Ewald summation, the maximum number of reciprocal-space vectors, K_{max} , was set equal to $\text{int}(\kappa \times L_{\text{box}}) + 1$. For the simulations at low reduced temperatures, very large vapor boxes were employed, and the cutoff for the real-space part was adjusted to be about 40% of the typical box length. Because the number density is small in the vapor box at lower-reduced temperatures, using a larger cutoff results in a minimal increase in the computational overhead for the real space part of the Ewald sum but significantly reduces the computational overhead of the reciprocal space part of the calculation.

The canonical version of the Gibbs ensemble^{73,74} employs two boxes in thermodynamic contact, without a direct interface. Molecules are swapped between the boxes to equilibrate the chemical potential, volume exchange moves are employed to equilibrate the pressure, and translational and rotational moves are used to reach thermal equilibrium. The liquid-phase box size was significantly larger than $2r_{\text{cut}}$. The size of the vapor box was adjusted during the equilibration period, so that, on average, approximately 20–40 molecules could be found in the vapor phase. The volume move probability was adjusted to have approximately one volume move accepted for every 10 MC cycles (1 MC cycle consists of N moves, where N is the number of molecules in the system). The swap moves employed configurational-bias Monte Carlo strategies,^{77,78} and the move probability and number of regrowth directions were adjusted to have approximately one move accepted for every 10–50 MC cycles, with higher numbers for lower reduced temperatures. The remaining move probabilities were equally divided between the translational and rotational moves. At any state point, 40000 MC cycles were used to equilibrate the system before starting the production runs. The production runs consisted of at least 40000 MC cycles at any state point. Each production run was divided into five blocks to compute statistical uncertainties (the standard deviations).

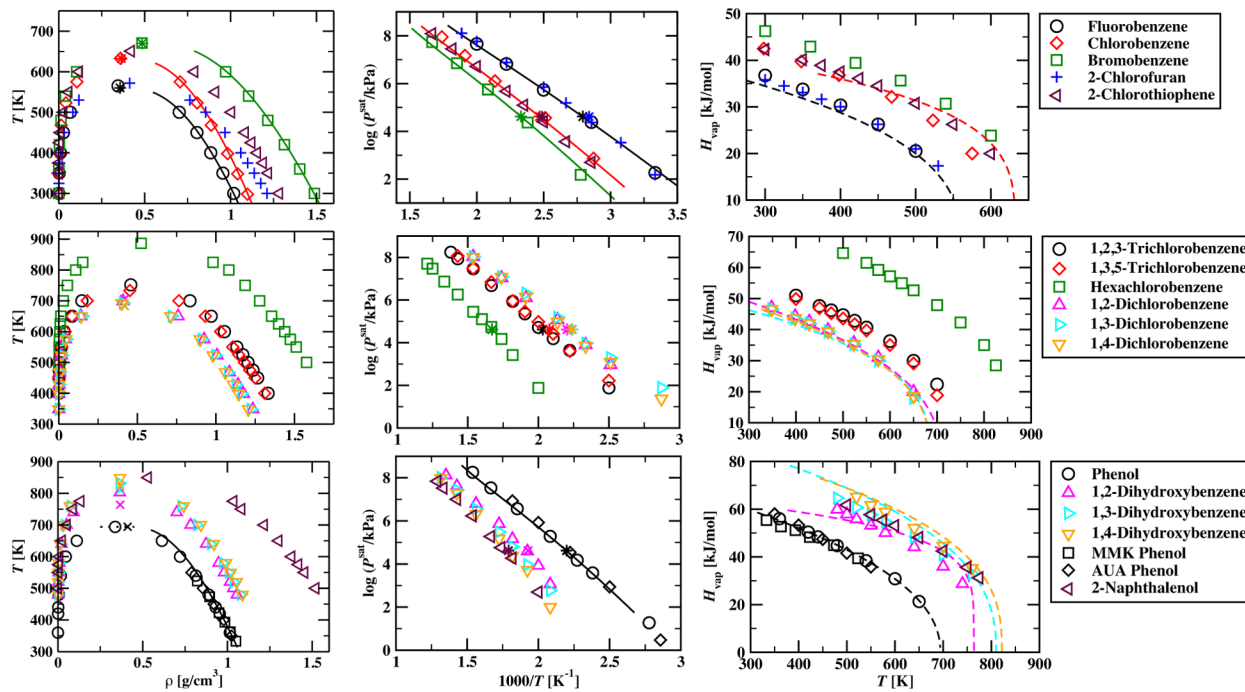


Figure 1. Vapor–liquid coexistence curves (first column), Clausius–Clapeyron plots (second column), and heat of vaporization curves (third column) for compounds with a single halogen substituent (top row), with multiple halogen substituents (middle row), and with hydroxy substituents (bottom row). Simulation data for the Trappe-EH force field and for the MMK and AUA phenol models^{86,87} are presented as indicated in the legends. The experimental critical points and normal boiling points⁸⁵ are shown as stars of the corresponding colors or as a horizontal dotted line when only T_c is available. The crosses of the corresponding colors indicate the critical points and normal boiling points taken from *Knovel Critical Tables*.⁸⁴ The solid and dashed lines of the corresponding colors indicate data from *Perry's Chemical Engineers' Handbook*⁹⁶ and *Knovel Critical Tables*,⁸⁴ respectively.

From the VLCC data, the critical temperature, T_c , and critical density, ρ_c , were computed using the density scaling law and the law of rectilinear diameter, respectively, with the scaling exponent, β^* , set to 0.325.^{79–81} The normal boiling point, T_b , was computed by the Clausius–Clapeyron equation using only the three or four temperatures closest to the boiling point.

Because polar aromatic molecules tend to have significant orientational ordering in the liquid phase, the conventional radial distribution function is not sufficient to illustrate their microstructure. Hence, an angle-dependent radial distribution function, $g(r,\theta)$ (ARDF), was used to provide concomitant information on the angular as well as the radial ordering in the liquid phase. The distribution function for a binary system, $g_{A,B}(r,\theta)$, is defined as

$$g_{A,B}(r,\theta) = \left\langle \frac{V}{N_A N_B \Delta V(r,\theta)} \sum_{i=1}^{N_A} \sum_{j=1}^{N_B} \delta(r - r_{ij}) \delta(\theta - \theta_{ij}) \right\rangle \quad (2)$$

where N_A and N_B are the numbers of molecules of types A and B, respectively; V , r_{ij} and θ_{ij} are the system volume, the center-of-mass distance between molecules i and j , and the angle formed by two characteristic molecular axes, such as the normal to the molecular plane or a bond vector, between molecules i and j , respectively. The differential volume element, $\Delta V(r,\theta)$, is given by $\frac{2}{3}\pi[(r + \Delta r)^3 - (r^3)][\cos(\theta) - \cos(\theta + \Delta\theta)]$, where Δr and $\Delta\theta$ are the resolutions of the distance and angle grids, respectively. The angular brackets represent an ensemble average.

3.2. VLCC for Binary Systems. The canonical version of the GEMC approach⁷⁴ was used to compute the VLCC for

benzene/benzonitrile and benzene/phenol, whereas the isothermal–isobaric version of the Gibbs ensemble⁷⁴ was used for the binary system of methanol/naphthalene. The systems consisted of either 500 or 1000 molecules. The move probabilities were set in the same manner as for the simulations for the neat systems. The systems were equilibrated for at least 50000 MC cycles, and an additional 50000–100000 MC cycles were used for production. The production runs were divided into five equal blocks to calculate averages and standard deviations.

In binary systems, molecules can be preferentially self-solvated or preferentially solvated by molecules of the other type, resulting in microheterogeneity of the liquid phase. To quantify such microheterogeneity, the local mole fraction variation ($x_{\text{local}}/x_{\text{bulk}}$) for a particular molecule type as a function of distance was calculated. The local mole fraction variation of molecule type A, LMFV_{AA}(r), is defined as

$$\text{LMFV}_{AA}(r) = \frac{1}{x_A} \left[\frac{\text{NI}_{AA}(r)}{\text{NI}_{AA}(r) + \text{NI}_{AB}(r)} \right] \quad (3)$$

where NI_{AX}(r) and x_A are the number of molecules of type X (A or B) within a center-of-mass distance r of a molecule of type A and the bulk mole fraction of type A, respectively. At very short separation, the LMFV is strongly biased by the size of the two types of molecules and might not represent a preferential interactions. Thus, LMFV data are only reported for center-of-mass separations where the sum in the denominator is larger than 0.5.

4. RESULTS AND DISCUSSION

4.1. Halogen-Substituted Rings. The VLCCs, saturated vapor pressure curves (SVPCs), and heat of vaporization curves (HOVCs) for fluorobenzene, chlorobenzene, and bromobenzene are presented in Figure 1, and the corresponding numerical values for the critical constants, T_c and ρ_c , and normal boiling points, T_b , are listed in Table 2. The simulation

Table 2. Critical Constants and Normal Boiling Points for Substituted Benzenes and 5-Membered Rings^a

compound	method	T_c (K)	ρ_c (kg/m ³)	T_b (K)
fluorobenzene	TraPPE-EH	565 ₃	345 ₅	360 ₂
	OPLS-AA	540 ₃	353 ₆	351 ₂
	expt	560	357	358
chlorobenzene	TraPPE-EH	633 ₃	359 ₄	402 ₁
	OPLS-AA	619 ₃	368 ₅	393 ₂
	expt	632	365	405
bromobenzene	TraPPE-EH	671 ₂	484 ₄	430 ₁
	OPLS-AA	677 ₄	496 ₇	431 ₁
	expt	[670]	[485]	429
1,2-dichlorobenzene	TraPPE-EH	699 ₄	409 ₆	454 ₂
	expt	[705]	[418]	454
1,3-dichlorobenzene	TraPPE-EH	693 ₃	409 ₄	447 ₂
	expt	[684]	[418]	446
1,4-dichlorobenzene	TraPPE-EH	692 ₃	402 ₅	454 ₂
	expt	[685]	[418]	447
1,2,3-trichlorobenzene	TraPPE-EH	752 ₆	458 ₉	491 ₂
	expt	n/a	n/a	492
1,3,5-trichlorobenzene	TraPPE-EH	733 ₄	452 ₉	486 ₂
	expt	n/a	n/a	481
hexachlorobenzene	TraPPE-EH	887 ₅	524 ₁₀	600 ₂
	expt	n/a	n/a	598
2-chlorofuran	TraPPE-EH	571 ₂	413 ₄	357 ₁
	expt	n/a	n/a	352 ₂
2-chlorothiophene	TraPPE-EH	653 ₂	420 ₂	408 ₁
	expt	n/a	n/a	402, 466
phenol	TraPPE-EH	694 ₄	337 ₅	455 ₁
	OPLS-AA	665 ₅	342 ₈	434 ₄
	expt	694.3	[411]	455
1,2-dihydroxybenzene	TraPPE-EH	808 ₅	370 ₇	527 ₂
	expt	[764]	[367]	519
1,3-dihydroxybenzene	TraPPE-EH	832 ₅	364 ₆	545 ₂
	expt	[810]	[367]	550
1,4-dihydroxybenzene	TraPPE-EH	849 ₄	366 ₄	558 ₃
	expt	[822]	[367]	558
benzonitrile	TraPPE-EH	686 ₄	315 ₄	463 ₂
	OPLS-AA	704 ₃	312 ₃	460 ₂
	expt	699	313	464
<i>p</i> -benzoquinone	TraPPE-EH	696 ₅	358 ₆	451 ₂
	expt	n/a	n/a	453 ₃
MUPE (TraPPE-EH)		0.7% [2.2%]	1.9% [3.5%]	0.6%

^aExperimental data taken from the NIST Chemistry Webbook.⁸⁵ Square brackets indicate data from *Knovel Critical Tables*.⁸⁴ First MUPE value computed over the set of compounds for which experimental data are available; second computed with respect to the data in *Knovel Critical Tables*. Subscripts denote the standard deviation in the last digit for the simulation data.

data (ρ_{liq} , ρ_{vap} , p_{vap} and ΔH_{vap}) for each compound are provided in the Supporting Information. The agreement of the simulation results for these three compounds included in the parametrization set for the TraPPE-EH force field with the experimental data for the saturated liquid densities and vapor pressures over the entire temperature range is excellent, with mean unsigned percentage errors (MUPEs) of less than 1% and 10%, respectively. The percentage errors for the T_b values of fluorobenzene, chlorobenzene, and bromobenzene are 0.6%, 0.7%, and 0.2%; the corresponding errors for T_c are 0.9%, 0.1%, and 0.1%; and those for ρ_c are 3.4%, 1.6%, and 0.2%, respectively. Although the deviations for ρ_c are somewhat larger, the percentage errors for the saturated liquid densities at a temperature close to 300 K, at 0.1%, 0.2%, and 0.2% for fluorobenzene, chlorobenzene, and bromobenzene, respectively, are very small.

For comparison, the vapor–liquid equilibria of these three halobenzenes were also determined here for the OPLS-AA force field^{82,83} (see numerical data in Table 2), and the resulting MUPEs for T_c and T_b are 2.2% and 1.8%, respectively, compared to MUPE values of 0.4% and 0.5%, respectively, for the TraPPE-EH force field.

Although the Clausius–Clapeyron slopes are well reproduced by the TraPPE-EH simulation data, there are significant differences between the calculated ΔH_{vap} values and those found in *Knovel Critical Tables*,⁸⁴ which are often based on correlations and group-additivity approaches and do not always reflect experimental data. For fluorobenzene, the TraPPE-EH force field yields ΔH_{vap} values that are somewhat larger (by less than 2 kJ/mol) at the lower temperature, but the shapes of the HOVCs are in good agreement. For chlorobenzene, the Knovel data yield a shape that differs significantly from the typical shape found for other halobenzenes and substituted benzenes, and it is likely that the TraPPE-EH values are more accurate.

Additional simulations were carried out for the three isomers of dichlorobenzene to assess the transferability of LJ parameters for the chlorine substituent atom, and their VLCCs, SVPCs, and HOVCs are also included in Figure 1. For these disubstituted benzenes, which are solids at room temperature, the experimental VLE data are limited to T_b . The TraPPE-EH predictions for the ortho and meta isomers agree with experiment to within the statistical uncertainty, but the T_b value of the para isomer is overpredicted by 7 K, and the resulting MUPE for the three dichlorobenzene isomers is 0.6%. The TraPPE-EH predictions for T_c and the data in *Knovel Critical Tables* agree within better than 1.5%, but the differences for ρ_c are somewhat larger, where *Knovel Critical Tables* lists the same value for all three isomers (as expected for a group-additivity approach). The heats of vaporization predicted by the TraPPE-EH force field and the data obtained from the correlation⁸⁴ are in excellent agreement for the ortho and para isomers, with maximum deviations of not more than 2% over the entire temperature range, but the correlation data for 1,3-dichlorobenzene start to deviate from the simulation data at lower temperatures. Transferability of the chlorine substituent atom was further tested by carrying out simulations for 2-chlorofuran and 2-chlorothiophene. The only reliable experimental data available for these molecules are the normal boiling points. TraPPE-EH predicts the normal boiling points with errors of 1.4% and 1.5% for 2-chlorofuran and 2-chlorothiophene, respectively. The NIST Chemistry Webbook⁸⁵ provides two widely different values (402 and 466 K)

for the boiling point of 2-chlorothiophene. The TraPPE-EH prediction confirms that the 466 K value is erroneous.

4.2. Hydroxy-Substituted Rings. For the hydroxyl substituent group, only the LJ parameters for the oxygen atoms were fit to experimental VLE data for phenol, whereas the LJ parameters for the polar hydrogen atom were taken without change from those developed for aromatic heterocycles (e.g., pyrrole).⁴³ Preliminary simulations of phenol using the CM4 charges indicated a lack of H-bonding in the liquid phase. To remedy this problem, the partial charge for the polar hydrogen was taken from the TraPPE-UA force field for alkanols.⁴⁹ The difference between the CM4 charge for the polar hydrogen in phenol and the TraPPE-UA force field ($\Delta q_H = +0.116$) was compensated by adding $-\Delta q_H$ to the CM4 charge value for the oxygen atom in phenol. The same Δq_H value was applied to the CM4 charges for the dihydroxybenzene isomers.

The bottom row of Figure 1 presents the VLCCs, SVPCs, and HOVCs for phenol, dihydroxybenzene isomers, and naphthalen-2-ol. Selected numerical data for these compounds are provided in Table 2. The new TraPPE-EH model for phenol reproduces the experimental data for T_b and T_c , whereas the predicted ρ_c value differs by nearly 20% from the value listed in *Knovel Critical Tables*.⁸⁴ This latter value might be based on a group-contribution estimate because oxygen-containing compounds tend to easily decompose at elevated temperatures and present a significant challenge in the determination of the critical properties. We believe that the value for ρ_c predicted by the TraPPE-EH model is more accurate than the value in *Knovel Critical Tables* because the TraPPE-EH model reproduces the overall shape of the VLCC very well.

For phenol, a number of other force fields are available for which simulation results for the thermophysical properties have been reported in the literature.^{86,87} Mooney et al. developed an all-atom model (henceforth referred to as the MMK model) and reported liquid-phase thermodynamic properties for temperatures up to 523 K,⁸⁶ whereas Ferrando et al. developed an anisotropic united-atom force field (henceforth referred to as the AUA model) for alcohols, including phenol, and reported VLE data for temperatures up to 550 K.⁸⁷ For ρ_{liq} at low reduced temperatures, all three force fields perform exceptionally well. At higher temperatures, however, the AUA force field underpredicts ρ_{liq} by 4% (at 550 K), whereas the MMK force field underpredicts it by 3% (at 523 K). A similar trend is seen for the TraPPE-EH force field, which underpredicts ρ_{liq} by 2.5% (at 540 K), although the error increases to 5% at 650 K, the highest temperature ($0.95T_c$) for which the simulations were carried out in the present work. The normal boiling point is predicted with errors smaller than 1% by the AUA and TraPPE-EH force fields. For the AUA force field, the error in the saturated vapor pressure increases from 7% at 350 K to 29% at 550 K.⁸⁷ In contrast, the TraPPE-EH force field predicts vapor pressures within 10% of the experimental value for all temperatures ranging from 360 to 650 K. The accuracies of the predicted ΔH_{vap} values are comparable for all three force fields. It is interesting to note that the “experimental” ΔH_{vap} values obtained from three different sources differ by as much as 5 kJ/mol. Mooney et al. compared to the experimental values from an older DIPPR database,^{86,88} Ferrando et al. compared to the DIPPR database released in 2005,^{87,89} and the present work uses the correlation found in *Knovel Critical Tables*.⁸⁴ The old

and new DIPPR databases differ by as much 5 kJ/mol, and the values from *Knovel Critical Tables* fall between them.

To test the transferability of the LJ parameters for the hydroxyl group attached to the benzene ring, additional simulations were carried out for 1,2-, 1,3-, and 1,4-dihydroxybenzenes (see Figure 1). For the dihydroxybenzenes, the experimental VLE data are limited to the normal boiling points, which are overpredicted by 6 K, underpredicted by 5 K, and spot on, respectively, for the three isomers, with their order correctly reproduced (see Table 2). Compared to the data in *Knovel Critical Tables*,⁸⁴ the TraPPE-EH model yields T_c values that are always higher (by ~3%). The TraPPE-EH model and *Knovel Critical Tables* yield nearly identical ρ_c values for all three isomers. Near T_b , the TraPPE-EH model yields ΔH_{vap} values that are larger, smaller, and right on the correlations for 1,2-, 1,3-, and 1,4-dihydroxybenzene, respectively. Furthermore, it should be noted that the shape of the HOVC for the ortho isomer from the *Knovel* correlation differs significantly from those for the other two isomers and phenol.

Additional simulations were carried out for naphthalen-2-ol to test the transferability of the hydroxyl group attached to the fused rings. The TraPPE-EH predictions for T_c , ρ_c , and T_b are reported in Table 3, and VLCCs are presented in Figure 1. As with the other fused-ring compounds, limited experimental data are available for naphthalen-2-ol. The experimental T_b ranges from 559 to 568 K,⁸⁵ and the TraPPE-EH value (567 K) falls within the range.

The local structures of phenol and the three dihydroxybenzene isomers in the liquid phase near their boiling points were investigated by intermolecular oxygen–oxygen radial distribution functions (RDFs) and number integrals (NIs). In contrast to those of alcohols with similar molecular weights,^{49,50} the RDFs for all the four molecules show a less pronounced first peak at a separation of about 2.9 Å (see Figure 2). In the case of phenol, there is only a very weak secondary peak at a separation of 5.2 Å, indicating the absence of aggregation in the liquid phase near its normal boiling point. The dihydroxy isomers show a more pronounced second peak and also a substantial third peak at separations of about 5.2 and 7.7 Å, respectively, suggesting the presence of some aggregation. The integration of the first peaks yields coordination numbers of 1.8, 3.1, 2.6, and 2.7 for phenol and 1,2-, 1,3-, and 1,4-dihydroxybenzene, respectively.

Because RDFs and NIs suggest the presence of H-bonding and some aggregation in hydroxybenzene, further analysis of the H-bonding and aggregation was carried out. We employed the same set of geometric criteria to define a H-bond as in a previous investigation of 1-hexanol in *n*-hexane mixtures.⁹⁰ This is a combined distance/angle metric according to which a H-bond exists when a pair of molecules satisfies the following criteria: $r_{OO} \leq 3.3$ Å, $r_{OH} \leq 2.5$ Å, and $\cos \theta_{OH...OL} \leq -0.1$, where r_{OO} , r_{OH} , and $\cos \theta_{OH...OL}$ are the O–O distance, the O–H distance, and the angle between the OH bond vector on the donating molecule and the oxygen–lone pair vector on the accepting molecule, respectively.

The numbers of H-bonds per molecule for phenol and 1,2-, 1,3-, and 1,4-dihydroxybenzene are 0.31, 0.81, 0.69, and 0.70, respectively; that is, the dihydroxybenzene isomers contain about twice the number of H-bonds as phenol. These relatively low numbers suggest that H-bonding is not as extensive as in the case of strongly aggregating molecules such as ethanol, which has about 1.7 H-bonds per molecule at a temperature close to its normal boiling point.⁹¹ Figure 3 shows the

Table 3. Critical Constants and Normal Boiling Points for Fused-Ring Compounds^a

compound	method	T_c (K)	ρ_c (kg/m ³)	T_b (K)
naphthalene	TraPPE-EH	750 ₃	320 ₃	490 ₂
	expt	748	320	490
anthracene	TraPPE-EH	895 ₁₀	528 ₁₅	614 ₂
	expt	n/a	n/a	613
phenanthrene	TraPPE-EH	897 ₆	539 ₁₄	615 ₂
	expt	869 ₁	n/a	613
naphthalen-2-ol	TraPPE-EH	850 ₆	533 ₁₁	567 ₁
	expt	n/a	n/a	559, 568
naphthalene-2-carbonitrile	TraPPE-EH	843 ₆	485 ₁₅	590 ₁
	expt	n/a	n/a	580 ₂
quinoline	TraPPE-EH	805 ₄	337 ₄	532 ₁
	expt	791	[348]	511
indole	TraPPE-EH	767 ₄	309 ₄	504 ₂
	expt	[794]	[329]	527
isoindole	TraPPE-EH	824 ₄	336 ₄	532 ₄
benzimidazole	TraPPE-EH	941 ₈	347 ₈	607 ₂
indazole	TraPPE-EH	863 ₄	352 ₅	553 ₆
purine	TraPPE-EH	952 ₄	392 ₅	613 ₄
benzo[b]thiophene	TraPPE-EH	771 ₄	355 ₄	494 ₆
benzo[c]thiophene	TraPPE-EH	768 ₄	358 ₄	490 ₂
benzoxazole	TraPPE-EH	740 ₅	372 ₅	478 ₁
benzisoxazole	TraPPE-EH	818 ₄	358 ₅	534 ₂
benzothiazole	TraPPE-EH	787 ₅	372 ₇	515 ₃
MUPE		1.8% [2.9%]	0.0% [3.2%]	1.4%

^aExperimental data taken from the NIST Chemistry Webbook.⁸⁵ Square brackets indicate data from *Knovel Critical Tables*.⁸⁴ First MUPE value computed over the set of compounds for which experimental data are available; MUPE value in square brackets computed with respect to the data in *Knovel Critical Tables*. Subscripts denote the standard deviation in the last digit for the simulation data.

distribution of molecules over H-bonded aggregate sizes. For phenol, nearly half of the molecules do not participate in H-bonding; the majority (roughly 35%) of aggregates have two molecules; and the fraction of molecules in aggregates larger than dimers falls off rapidly, with just under 2% of the molecules being found in pentameric aggregates. It is evident from Figure 3 that dihydroxybenzene isomers aggregate more strongly than phenol. Among the three dihydroxy isomers, 1,2-dihydroxybenzene has a slightly stronger preference for aggregates of size (n_{agg}) smaller than 5 compared to the other two isomers, whereas the opposite is true for $n_{\text{agg}} > 5$.

4.3. Benzonitrile, Naphthalene-2-carbonitrile, and p-Benzoquinone.

The VLE data for compounds with nitrile and

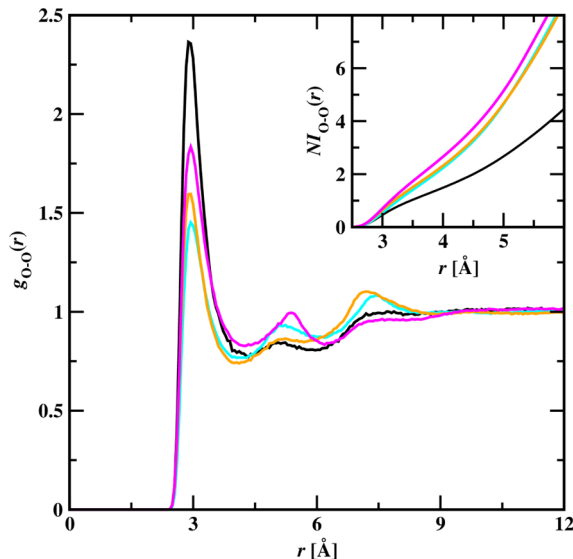


Figure 2. Intermolecular oxygen–oxygen radial distribution functions and number integrals (inset) for the saturated liquid phase of phenol at 480 K (black), 1,2-dihydroxybenzene at 520 K (magenta), 1,3-dihydroxybenzene at 520 K (cyan), and 1,4-dihydroxybenzene at 520 K (orange).

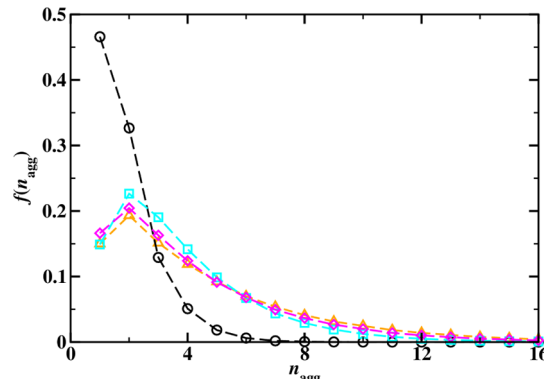


Figure 3. Fraction of molecules belonging to H-bonded aggregates of a given size in the liquid phases of phenol ($T = 480$ K) and dihydroxy isomers ($T = 520$ K). The black circles, cyan squares, magenta diamonds, and orange triangles represent the data for phenol and 1,2-, 1,3-, and 1,4-dihydroxybenzene, respectively.

carbonyl groups are graphically depicted in Figure 4, and numerical values for T_c , ρ_c , and T_b are provided in Tables 2 and 3. The LJ parameters for the carbon and nitrogen atoms of the nitrile group were fitted to reproduce the experimental saturated liquid densities and vapor pressures of benzonitrile. The TraPPE-EH model yields p_{sat} and ρ_{liq} values with MUPEs of 7.8% and 1.7%, respectively, over the temperature range from 300 to 640 K, but it should be noted that ρ_{liq} is overpredicted at the lower temperatures and underpredicted at the higher temperatures. T_b is underestimated by only 1 K, whereas T_c is underestimated by 2% and, possibly somewhat fortuitously, ρ_c falls within 1% of the experimental value. The predicted T_b value for naphthalene-2-carbonitrile falls 2% above the experimental value, but other experimental VLE data are not available for this compound. It should be noted here that the OPLS-AA model⁸³ for benzonitrile yields VLE data with accuracy similar to that of the TraPPE-EH force field.

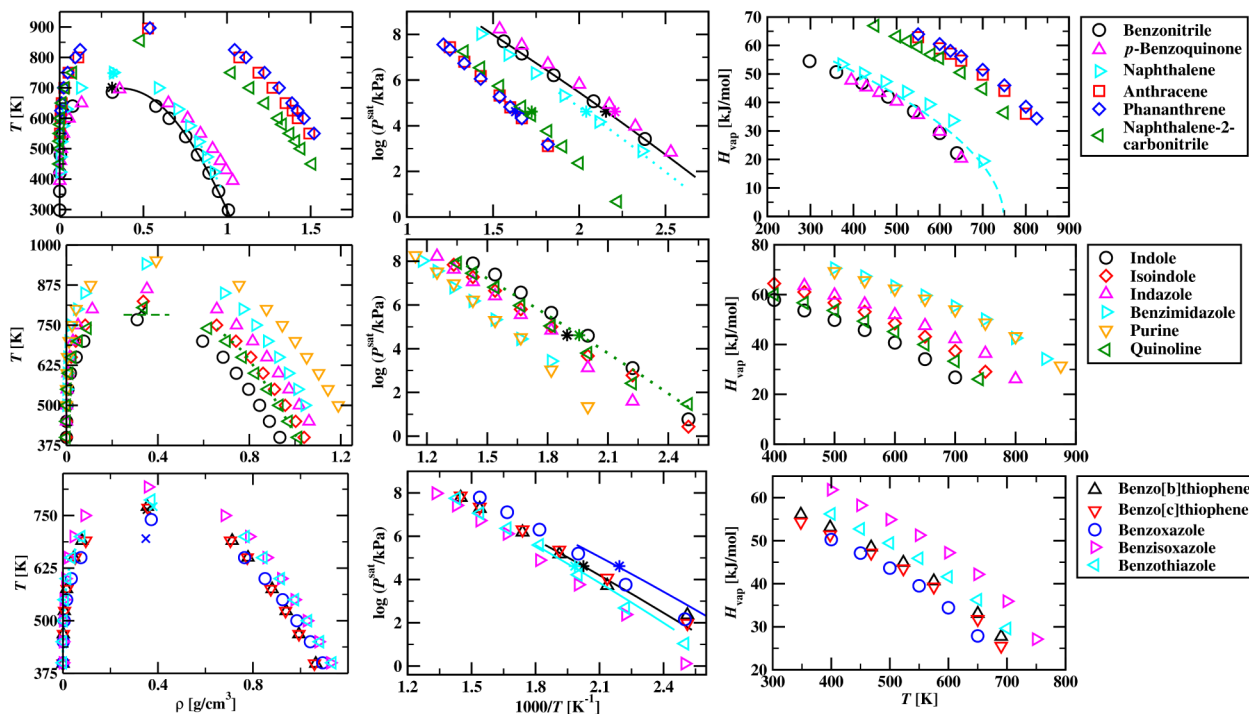


Figure 4. Vapor–liquid coexistence curves (first column), Clausius–Clapeyron plots (second column), and heat of vaporization curves (third column) for compounds with a nitrile or carbonyl substituent and polycyclic aromatic hydrocarbons (top row), for N-containing fused rings (middle row), and for S- and O-containing fused rings (bottom row). Simulation data for the TraPPE-EH force field are presented as indicated in the legends. The experimental critical points and normal boiling points⁸⁵ are shown as stars of the corresponding colors or as a horizontal dotted line when only T_c is available. The crosses of the corresponding colors indicate the critical points and normal boiling points taken from *Knovel Critical Tables*.⁸⁴ The solid, dashed, and dotted lines of the corresponding colors indicate data from *Perry's Chemical Engineers' Handbook*,⁹⁶ *Knovel Critical Tables*,⁸⁴ and experiments,^{97–99} respectively.

In the case of *p*-benzoquinone, the only experimental VLE data available are for T_b , and hence, solid-phase data in the form of the unit-cell parameters were also included in the training set to arrive at set of LJ parameters for the carbon and oxygen atoms of the carbonyl group. The TraPPE-EH force field reproduces T_b within 2 K, the experimental unit cell volume at 113 K⁹² is matched within 2%, and the six unit cell parameters yield an MUPE of 2%.

4.4. Naphthalene and Fused-Ring Heterocycles. The LJ parameters for the linker carbon atom between two fused aromatic rings were determined by fitting to ρ_{liq} and p_{sat} for naphthalene. The corresponding VLCC, SVPC, and HOVC are depicted in Figure 4, and the critical constants are provided in Table 3. Excellent agreement for the VLE properties is achieved by the TraPPE-EH model for naphthalene, with T_c , ρ_c , and T_b being reproduced within the statistical uncertainties of the simulation. Furthermore, ρ_{liq} is predicted with an MUPE of 0.2% for temperatures up to 523 K. Compared to the correlation,⁸⁴ the TraPPE-EH model predicts slightly larger ΔH_{vap} values at intermediate temperatures, but the agreement is very good below 450 K (see Figure 4).

This is a significant improvement over previous models for naphthalene. Although the TraPPE-UA force field yields an equally good prediction for T_c and ρ_c , it significantly underestimates the normal boiling point by more than 5%.⁴⁷ The AUA model for naphthalene predicts T_c , ρ_c , and T_b with errors of 1.9%, 5.0%, and 0.9%, respectively, but overestimates ρ_{liq} by about 3% near T_b .³⁷

The transferability of the LJ parameters for the linker carbon atom and N, O, and S heteroatoms was assessed by computing the vapor–liquid equilibria for a large set of fused-ring

heterocycles, including six heterocycles with only N heteroatoms (although experimental VLE data are available for only two of them) and five additional heterocycles containing O, S, and/or N heteroatoms (although experimental VLE data are available for only three of them). The VLE curves for quinoline, the only compound with two six-membered rings, are shown in Figure 4. Although the ρ_{liq} values are in satisfactory agreement with the experimental data over a wide temperature range, p_{sat} is significantly underpredicted at all temperatures (with the deviation increasing at low reduced temperature). As an outcome, T_b and T_c are overpredicted by 4% and 2%, respectively.

Experimental VLE data for other N-containing fused-ring heterocycles are extremely scarce because these compounds are solids at room temperature. The VLE curves for indole, isoindole, indazole, benzimidazole, and purine are depicted in Figure 4. To our knowledge, an experimental value for T_b is available only for indole. In contrast to what was found for quinoline, the TraPPE-EH force field significantly underestimates T_b by about 5% for indole and, hence, must overestimate its vapor pressure. In addition, the TraPPE-EH prediction for T_c is about 30 K lower than the correlation value reported in *Knovel Critical Tables*.

The TraPPE-EH force field predicts that ρ_{liq} , T_c , and T_b are about 7% larger for isoindole than for indole. Additional nitrogen heteroatoms lead to further upward shifts in the VLCCs for indazole, benzimidazole, and purine (see Figure 4).

Most of the fused rings considered in the present work do not contain both H-bond donors and acceptors, but indazole, benzimidazole, and purine (purine derivatives are one of the key constituents of nucleic acids) are the exceptions (see Figure

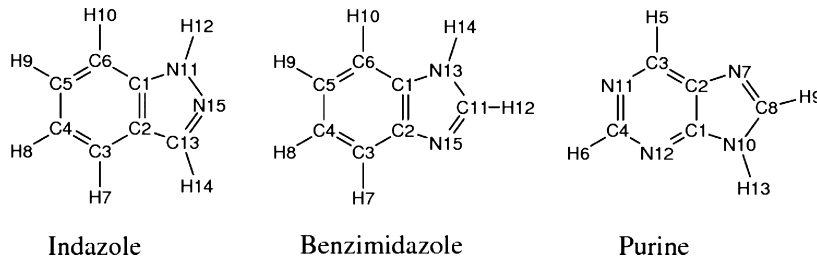


Figure 5. Atom numbering for selected fused-ring heterocycles.

5). Hence, additional simulations at $T = 500$ K and $p = 101.3$ kPa in the isobaric–isothermal ensemble were carried out for these molecules to elucidate the arrangement of the molecules in the liquid phase. Indazole and benzimidazole contain one polar hydrogen and two possible acceptor sites, whereas purine contains one polar hydrogen and four possible acceptor sites (see Figure 5 for the atom numbering used in this work). Because the number of acceptors is larger than the number of donors, there is a competition for the available polar hydrogens. Figure 6 shows the pair correlation functions and correspond-

of these fused rings, but it should be noted that H-bonds for ammonia are also very weak.⁵⁷

Purine, with three basic nitrogens present in the ring, displays slightly different behavior. The heights of the first peaks for the basic nitrogens are much lower than those found for indazole and benzimidazole. The N7 and N11 nitrogen atoms of purine are equally likely to be involved in a H-bond, whereas the propensity for H-bond formation with N12 is significantly smaller. As in the cases of indazole and benzimidazole, the first peak for the N7—H13, N11—H13, and N12—H13 pairs is located at approximately 2.2 Å. Again, from the corresponding number integrals it is evident that the propensity for H-bond formation is relatively low.

Additional structural details regarding the orientation of molecules in the first coordination shell was obtained from the ARDFs. Figure 7 shows $g(r,\theta)$ distributions for indazole, benzimidazole, and purine, where the distance is based on center-of-mass separations and two different characteristic axes, one along the normal to the plane and the other along the long axis of the molecule, are considered for angle determination. From $g(r,\theta)$, one immediately notices that all three molecules have a strong preference for parallel orientation in the first coordination shell, with ordering being more dominant in purine than in the other two molecules. It is particularly noteworthy that purine exhibits the most pronounced peaks in the ARDF, whereas the peak height in the RDF is smaller than for other compounds; that is, the preference for parallel alignments is stronger for purine, and the repulsive core is more extended for all other orientations. There is a small peak for the perpendicular orientation at somewhat larger r values for the benzimidazole and indazole liquid phases, with the perpendicular orientation being more pronounced in the case of benzimidazole than imidazole. As the dipole-moment vector of these molecules lies in the plane of the molecule, a vector along the long axis was chosen to define the second characteristic axis of the molecule. The long axis was defined by the vectors pointing from C5 to C1, from C11 to H12, and from N11 to C2 for indazole, benzimidazole, and purine, respectively. For the indazole liquid phase, there is one prominent peak at $r \approx 5.2$ Å and $\theta \approx 170^\circ$ and two smaller peaks at $r \approx 4.8$ Å and $\theta \approx 20^\circ$ and at $r \approx 6.2$ Å and $\theta \approx 90^\circ$. This suggests that nearest-neighbor molecules prefer to align with pyrazole rings pointing toward each other. The $g(r,\theta)$ distribution for benzimidazole shows two rather broad peaks centered at around 30° and 150° for $4.8 < r < 5.2$ Å, indicating that benzimidazole molecules align with an angle that maximizes the H-bonding between the N15 and H14 atoms. In the case of purine, one would expect that molecules can maximize the H-bonding of N11 and N12 with H13 by having the pyrazole ring point to the pyrimidine ring and maximize the H-bonding of N7 with H13 by aligning in antiparallel

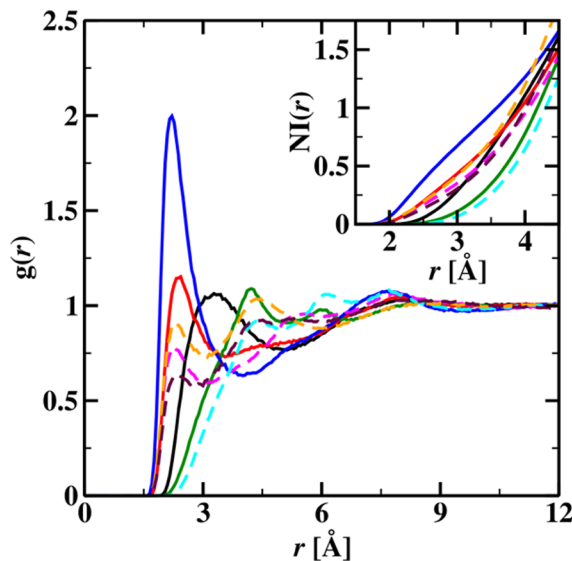


Figure 6. Radial distribution functions and corresponding number integrals for indazole, benzimidazole, and purine. For indazole, the solid black and red lines represent the N11—H12 and N15—H12 pairs, respectively; for benzimidazole, the solid green and blue lines represent the N13—H14 and N15—H14 pairs, respectively; and for purine, the dashed magenta, cyan, orange, and maroon lines represent the N7—H13, N10—H13, N11—H13, and N12—H13 pairs, respectively. For unit numbers, refer to Figure 5.

ing number integrals for all combinations of polar hydrogen and acceptor sites. In the case of indazole and benzimidazole, there is a clear preference for the basic nitrogen as opposed to the acidic nitrogen. The first peak of the radial distribution function for N15—H12 in indazole and N15—H14 in benzimidazole occurs at approximately 2.2 Å. The peak is higher for the N15—H14 pair in the benzimidazole molecule than for the N15—H12 pair in the indazole molecule, pointing to enhanced ordering among the nearest neighbors. The corresponding number integrals show that less than one hydrogen atom can be found within $r < 3$ Å (a fairly lax upper bound for a H-bond) around the basic nitrogen atoms. This might be due to the steric hindrance presented by the bulkiness

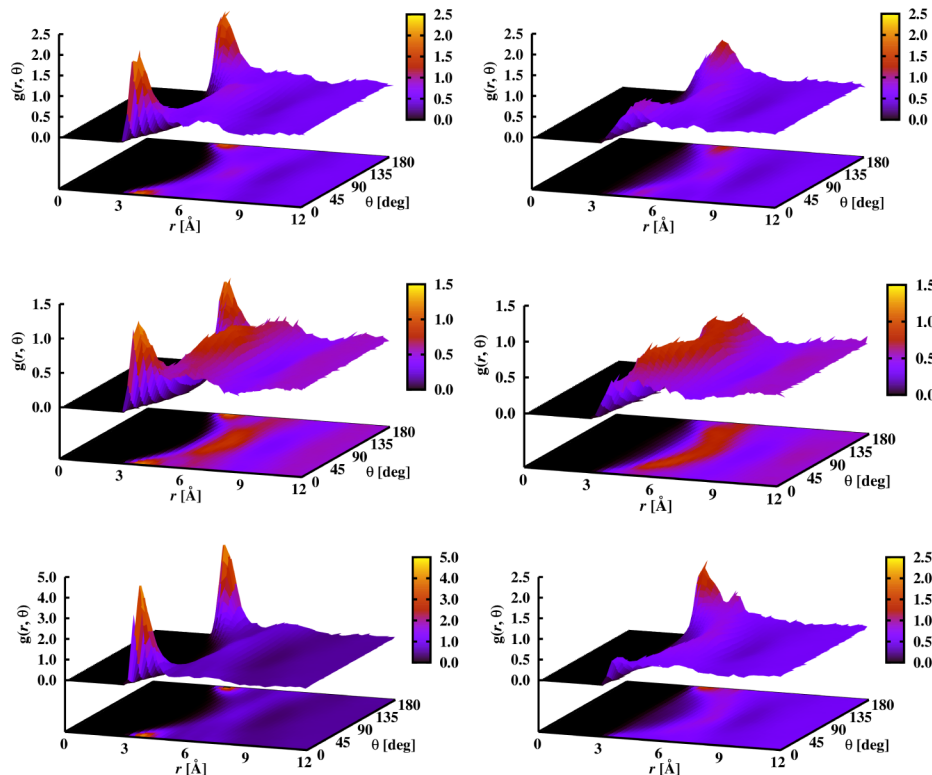


Figure 7. Angular–radial distribution functions for indazole (top), benzimidazole (center), and purine (bottom). The distances are based on center-of-mass separations, whereas the angles are based on the normal to the plane of the molecules (left) and on vectors along the long axis of the molecule (right). The long axis is defined by the vectors along C5—C1, C11—H12, and N11—C2 for indazole, benzimidazole, and purine, respectively. For unit numbers, refer to Figure 5.

configurations. Not surprisingly, $g(r,\theta)$ in Figure 7 shows a prominent peak at approximately 180° .

4.5. Phase Behavior and Microscopic Structure of Binary Systems. The very good performance of the TraPPE-EH force field in predicting single-component thermophysical properties led us to examine the effectiveness and accuracy of the developed potentials in an array of binary systems that are representative of different types of dominant interactions observed in aromatic systems, namely, those for weakly polar compounds arising from dispersive, quadrupole–multipole, and π – π stacking interactions and those for strongly polar compounds including dipole–multipole and H-bonding interactions in addition to the other three types found for weakly polar compounds. Based on the availability of experimental data for comparison purposes, three different binary systems were selected for investigation: benzene/benzonitrile (weakly polar/strongly polar), benzene/phenol (weakly polar/strongly polar including H-bonding), and methanol/naphthalene (strongly polar including H-bonding/weakly polar).

4.5.1. Binary Mixture of Benzene and Benzonitrile. The predictions for the pressure–composition diagram for the benzene/benzonitrile mixture at $T = 353.15\text{ K}$ are compared to the experimental data⁹³ in Figure 8. The agreement with experiment is good for the entire composition range, as pressures measured experimentally fall within the error bars of the simulation data, except for the bubble-point composition corresponding to a benzene mole fraction of 0.19. From Figure 8, it is evident that the separation factor is large at all of the pressures for which the simulations were performed. For example, the liquid phase with $x_{\text{benzene}} \approx 0.1$ is in equilibrium

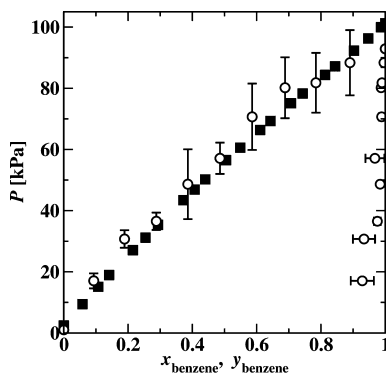


Figure 8. Pressure–composition diagram for the benzene/benzonitrile mixture at $T = 353.15\text{ K}$. The solid squares and open circles represent the experimental data⁹³ and simulation results, respectively. The error bars are shown only if larger than the symbol size, and for clarity, pressure error bars are shown only for the bubble-point predictions.

with a vapor phase with $y_{\text{benzene}} > 0.9$. This indicates that the dipole–dipole interactions present in benzonitrile make a very substantial contribution to the cohesive energy compared to the quadrupolar and dispersive interactions that make up the cohesive energy for benzene. This is also suggested by the fact that the normal boiling point of benzonitrile predicted by the TraPPE-EH force field is about 110 K higher than the normal boiling point of benzene, whereas that of ethylbenzene falls midway between the two.

The liquid-phase benzene–benzene and benzonitrile–benzonitrile LMFVs for $x_{\text{benzene}} \approx 0.2$ and 0.8 are shown in Figure 9. At short distances, $r < 5.5\text{ \AA}$, there is a sharp depletion

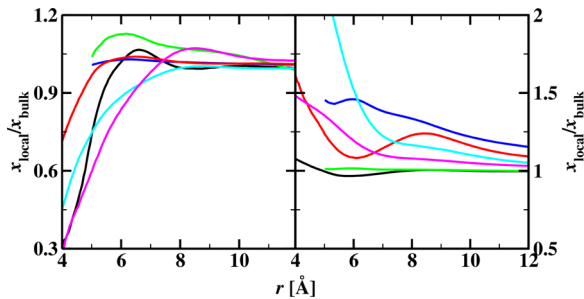


Figure 9. Local mole fraction variations for arene–arene (left) and polar–polar (right) pairs in the liquid phases for the benzene/benzonitrile, benzene/phenol, and naphthalene/methanol mixtures. The black, red, green, blue, magenta, and cyan lines represent the data for $x_{\text{benzene}} \approx 0.2$ and 0.8 for benzene/benzonitrile, for $x_{\text{benzene}} \approx 0.2$ and 0.8 for benzene/phenol, for $x_{\text{naphthalene}} \approx 0.4$ and 0.8 for naphthalene/methanol, respectively.

in the fraction of benzene molecules around other benzene molecules, whereas there is an enhancement for benzonitrile pairs; that is, there is preferential solvation of benzonitrile by other benzonitrile molecules. These deviations from ideal mixing are more pronounced when the mole fraction of benzonitrile, the polar compound, is small.

A better understanding of orientational and radial ordering in the liquid phase can be gained from ARDFs. For benzene, the characteristic axis is chosen to be the 6-fold rotational symmetry axis, normal to the plane of the ring. Benzonitrile, on the other hand, is characterized by two different axes, one along the dipole moment vector, coinciding with the CN bond vector, and the other normal to the plane of the benzene ring. The ARDFs for the pure benzene and benzonitrile liquid phases are shown in the top part of Figure 10. One immediately notices that the orientations of the molecules in the first solvation shell are correlated and the degrees of correlation are significantly different for benzene and benzonitrile. Additionally, within the first solvation shell, the radial distance between the center of mass of the molecules is larger when the benzene rings are in a perpendicular configuration rather than a parallel configuration, indicating better packing for the parallel configuration. In the first solvation shell of liquid benzene, there is a preference for parallel configurations for $3.4 < r < 5.2$ Å and for perpendicular configurations for $5.4 < r < 6.4$ Å. In addition to the packing arguments, at these center-of-mass separations, the respective configurations are energetically more

favorable.⁴³ For the benzonitrile liquid phase, the ARDFs illustrate an entirely different picture than found for benzene. The $g(r,\theta)$ distribution with the angle based on the normal to the plane of the benzene ring shows a very strong preference for parallel configurations and only a minor hump for perpendicular configurations. Additionally, $g(r,\theta)$ with the angle based on the dipole moment vector of the molecules shows a higher probability for antiparallel configurations among the nearest neighbors because it is energetically more favorable.

The lower part of Figure 10 shows ARDFs for the benzene/benzonitrile mixture with $x_{\text{benzene}} \approx 0.5$. It is evident that the orientational orderings of benzene around other benzene molecules and of benzonitrile around other benzonitrile molecules remain rather similar to those of the respective neat liquid phases. The ARDF for the benzene–benzonitrile pair suggests that the spatial distribution for the unlike pair is a combination of the distributions observed in neat benzene and neat benzonitrile. The benzene–benzonitrile ARDF retains the peaks near 0° and 180° found for benzonitrile and that around 90° found for benzene, but the peak heights are reduced compared to the ARDFs for the like pairs.

4.5.2. Binary Mixture of Benzene and Phenol. The ability of the TraPPE-EH force field to accurately represent the interactions between an aromatic compound with H-bond donor and acceptor sites and a weakly polar compound interactions was assessed through the prediction of the pressure–composition diagram for the benzene/phenol mixture at $T = 353.15$ K (see Figure 11). The agreement with experiment⁹⁴ for the bubble-point line is highly satisfactory, as the measured pressures for most of the compositions fall within the simulation uncertainties. The predictions for the dew-point compositions are also in good agreement with the experimental measurements. Because the phenol–phenol interactions are much stronger than the benzene–benzene interactions, the vapor phase consists mostly of benzene molecules.

The microheterogeneity of the benzene-rich and phenol-rich liquid phases was investigated through LMFVs (see Figure 9). The benzene–benzene LMFV for this mixture matches well those obtained for the benzene/benzonitrile mixture, showing a weak peak at $r \approx 6$ Å that decreases in height with increasing benzene mole fraction. The phenol–phenol LMFV exhibits much stronger enhancements in the first solvation shell, and the enhancement is more pronounced for the benzene-rich phase where it persists to $r > 12$ Å. This indicates that phenol

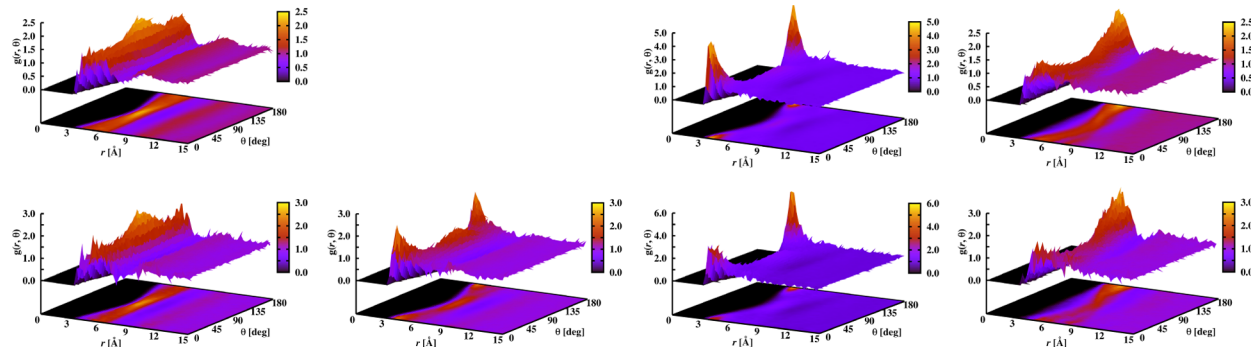


Figure 10. Angular–radial distribution functions for the liquid phase of the benzene/benzonitrile system. The top and bottom rows show ARDFs for neat phases and a phase with $x_{\text{benzene}} \approx 0.5$, respectively. Data for benzene–benzene, benzene–benzonitrile, and benzonitrile–benzonitrile pairs are shown from left to right, respectively. The orientation is defined by the angle between the normal vectors of the two planes given by the aromatic rings (first three columns) and by the angle between the dipole vectors of benzonitrile (right column).

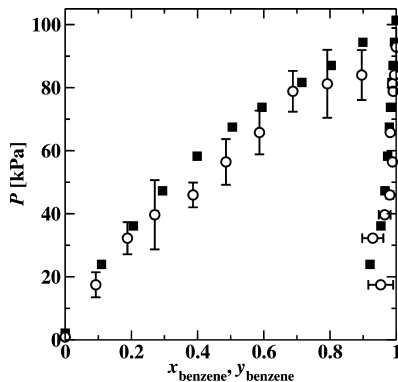


Figure 11. Pressure–composition diagram for the benzene/phenol mixture at $T = 353.15\text{ K}$. The solid squares and open circles represent the experimental data⁹⁴ and simulation results, respectively. The error bars are shown only if larger than the symbol size, and for clarity, pressure error bars are shown only for the bubble-point predictions.

molecules prefer to form extended aggregates. Figure 12 shows the O–O and O–H radial distribution functions and corresponding number integrals for $x_{\text{benzene}} = 0.0, 0.4$, and 0.7 . The presence of H-bonding at all three compositions is clearly evident in the prominent O–O and O–H peaks at 2.85 and 1.95 \AA , respectively, and the strong second peak at 3.5 \AA for the O–H RDF. Because of the formation of H-bonded aggregates, dilution by benzene leads to large enhancements of these peaks. Integration of the first peak in the O–O RDF yields coordination numbers of $1.9, 1.7$, and 1.0 for $x_{\text{benzene}} = 0.0, 0.34$, and 0.7 , respectively, and the corresponding coordination numbers from the O–H RDFs are $0.74, 0.62$, and 0.38 , respectively. As expected, an increase in x_{benzene} leads to fewer H-bonds per phenol molecule.

ARDFs for neat phenol at 353.15 K are shown in the top part of Figure 13. The ARDF with the angle determined by the normal vectors to the phenyl rings shows that the nearest-neighbor phenol molecules have a small preference for either parallel or perpendicular configurations, whereas the distribution function with the angle based on the CO bond vector indicates a preference for the antiparallel orientation. Figure 13 shows benzene–benzene, benzene–phenol, and phenol–phenol ARDFs for the liquid phase with $x_{\text{benzene}} \approx 0.5$. The benzene–benzene and benzene–phenol ARDFs indicate that nearest-neighbor molecules have a very small preference for perpendicular configurations, whereas the phenol–phenol

ARDF with the angle based on the normal to the ring yields a preference for perpendicular orientations. The phenol–phenol ARDF with the angle based on the CO bond vector shows that angles of more than 45° between CO bond vectors are more common, and the probability peaks for the two bond vectors pointing in opposite directions.

4.5.3. Binary Mixture of Naphthalene and Methanol.

Vapor–liquid compositions of naphthalene/methanol binary systems were calculated at $T = 579.75\text{ K}$ and different applied external pressures using the TraPPE-UA model for methanol⁴⁹ and the TraPPE-EH model for naphthalene. Figure 14 shows a comparison of the predicted pressure–composition diagram with the experimental data.⁹⁵ The composition of the methanol-rich (low-density) phase is predicted with very high accuracy, whereas the predictions for the composition of the naphthalene-rich phase are less satisfactory, with the methanol solubility being somewhat underestimated. The relative error in x_{methanol} does not change much as a function of pressure (whereas the absolute error is smaller at low pressure), and the deviations are likely caused by a slight underestimation of the favorable interactions between methanol and the π electrons, as one might expect from a nonpolarizable force field.

As can be seen in Figure 9, the LMFDs indicate a very strong preference for methanol molecules to be solvated by other methanol molecules particularly at low $x_{\text{methanol}} \approx 0.2$. Methanol is a small highly polar molecule that likes to form H-bonded aggregates. However, the methanol–methanol LMFD approaches unity relatively quickly; that is, the spatial extent of these dense methanol aggregates is limited. There is also a significant depletion of naphthalene in the solvation shell of a naphthalene molecule that is due to the very different sizes of the two molecules.

Because of the H-bonding nature of methanol and the bulkiness of naphthalene molecules, these mixtures display distinct orientational ordering as illustrated by the ARDFs calculated for the mixtures at $P = 5.12$ and 11.19 MPa (see Figure 15). The methanol–methanol ARDFs exhibit a preference for the O–H vectors to align in parallel configurations. The methanol–methanol ARDF for the lower methanol mole fraction shows a very strong peak near 0° , and the angles below approximately 90° are populated with higher probability. At the higher methanol mole fraction, the orientational distribution is broader, and angles smaller than 90° are more populated, with angles near 45° being most preferred. Naphthalene molecules, on the other hand, show a

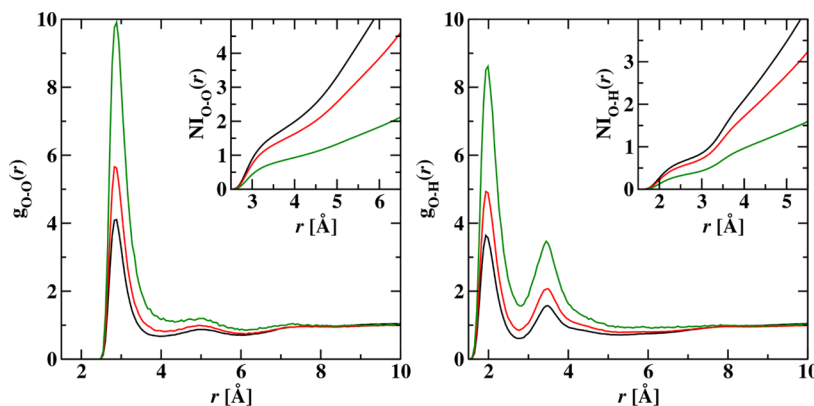


Figure 12. Radial distribution functions and number integrals for O–O and O–H in the liquid phase of the benzene/phenol system. The black, red, and green lines represent data for $x_{\text{benzene}} = 0.0, 0.4$, and 0.7 , respectively.

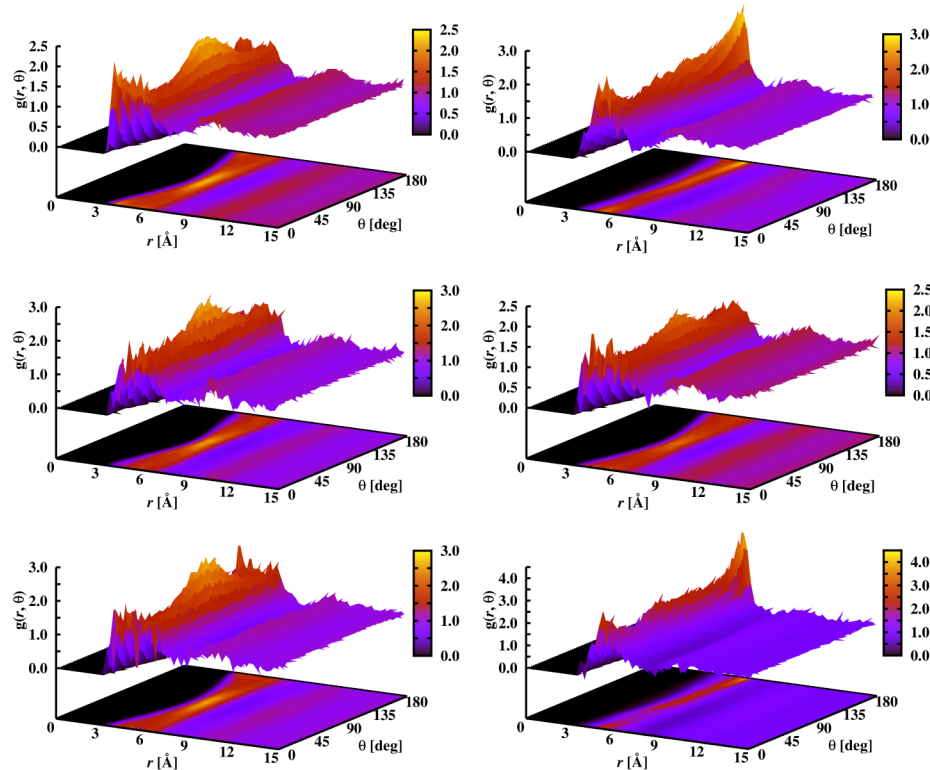


Figure 13. Angular–radial distribution functions for the liquid phase of the benzene/phenol system. The top row shows ARDFs for neat phenol obtained for the angle between the normal vectors to the aromatic rings (left) and the CO bond vectors of the two phenol molecules (right). The middle and bottom rows show ARDFs for a phase with $x_{\text{benzene}} \approx 0.5$. The angles were calculated between the normal to the aromatic rings for benzene–benzene pairs (center left), benzene–phenol pairs (center right), and phenol–phenol pairs (bottom left) and between the CO bond vectors of two phenol molecules (bottom right).

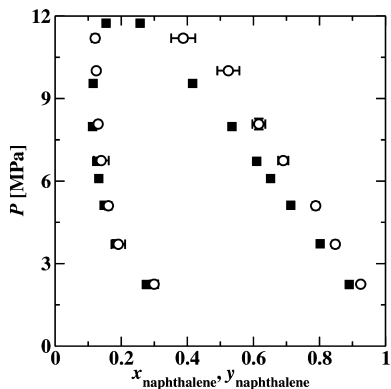


Figure 14. Pressure–composition diagram for the naphthalene/methanol mixture at $T = 579.75$ K. The solid squares and open circles represent the experimental data⁹⁵ and simulation results, respectively. The error bars are shown only if larger than the symbol size, and for clarity, pressure error bars are shown only for the bubble-point predictions.

strong preference for parallel orientations of the aromatic rings (parallel or antiparallel orientations for the normal vectors) within the first solvation shell, thereby optimizing the packing of these bulky molecules. This preference for parallel alignments is slightly stronger at the lower $x_{\text{naphthalene}}$ value. The methanol–naphthalene ARDF is nearly isotropic at all separations for both state points, indicating that methanol molecules tend to have nonspecific interactions with the naphthalene molecules.

5. CONCLUSIONS

Using the explicit-hydrogen version of the transferable potentials for phase equilibria (TraPPE-EH) force field for benzene and five- and six-membered aromatic heterocycles⁴³ as a starting point, the TraPPE-EH has been extended to various substituted aromatic compounds through the parametrization of the Lennard-Jones parameters for the exocyclic groups —F, —Cl, —Br, —OH, —C≡N, and = O and to fused-ring aromatic compounds through the parametrization of the aromatic linker carbon atom for two rings. The molecular structures, partial charges, and torsional potentials for all compounds were obtained from electronic structure calculations. The parametrization of the LJ terms was carried out using vapor–liquid phase equilibrium data, and the parametrization set included the following six compounds: fluorobenzene, chlorobenzene, bromobenzene, phenol, benzonitrile, and naphthalene. In addition, parameters for *p*-benzoquinone were fitted against its normal boiling point and crystal structure data. For validation purposes, the TraPPE-EH force field was then applied to (di-, tri-, and hexa-) chlorobenzenes, dihydroxybenzenes, quinoline, benzo[*b*]-thiophene, benzo[*c*]thiophene, benzoxazole, benzisoxazole, benzimidazole, benzothiazole, indole, isoindole, indazole, and purine.

Figure 16 provides a graphical summary of the accuracy of the TraPPE-EH force field for the prediction of vapor–liquid equilibrium properties of the aromatic compounds investigated here. In the figure, the TraPPE-EH predictions for saturated liquid densities, normal boiling points, critical temperatures, and critical densities are compared with the experimental data⁸⁵

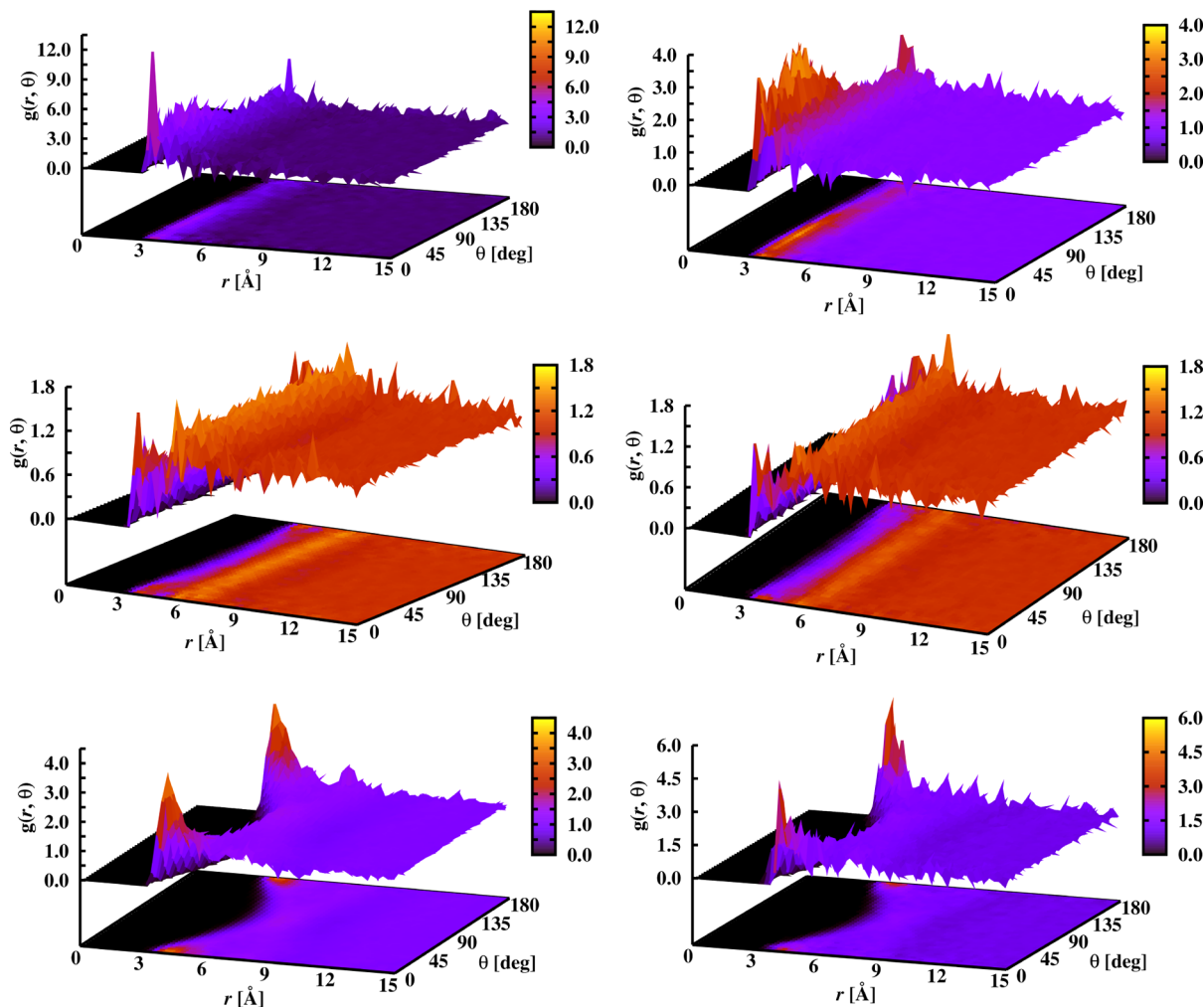


Figure 15. Angular–radial distribution functions for the liquid phase of the naphthalene/methanol system with $x_{\text{naphthalene}} \approx 0.77$ (left column) and 0.36 (right column). The top, center, and bottom rows show ARDFs for methanol pairs obtained for the angle between the two OH bond vectors, for naphthalene–methanol pairs obtained for the angle between the normal vector to the aromatic ring and the OH bond vectors, and for naphthalene pairs obtained for the angle between the normal vectors to the aromatic rings, respectively.

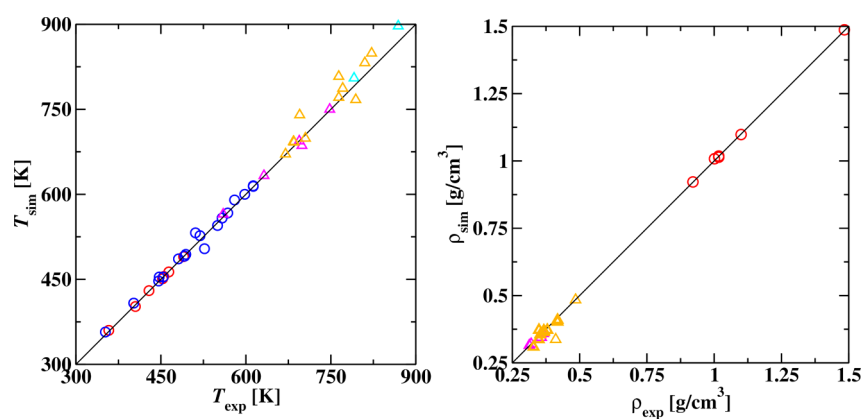


Figure 16. Correlation plots comparing the predictions for the TraPPE-EH model with literature data. (Left) Normal boiling points (circles) and critical temperatures (triangles), (right) near-ambient liquid densities (circles) and critical densities (triangles). The red and magenta symbols show data for compounds that were used in the parametrization process, the blue and cyan symbols represent data for the validation compounds with available experimental data,⁸⁵ and the orange symbols show compounds where the corresponding literature data are taken from *Knovel Critical Tables*.⁸⁴

and *Knovel Critical Tables*.⁸⁴ Least-squares analysis yields the following correlation coefficients, C , for the parametrization compounds: 0.999, 0.999, 0.996, and 0.988 for T_b , ρ_{liq} at near-

ambient conditions, T_c (excluding bromobenzene, for which an experimental value of T_c is not available), and ρ_c (excluding bromobenzene and phenol, for which experimental values of ρ_c

are not available), respectively. The corresponding regression coefficients (slopes) range from 0.790 (note small range of ρ_c values) to 1.002. For the validation compounds, experimental values are limited to T_b data for most compounds because these compounds tend to be solids at room temperature and thermally unstable at temperatures approaching their critical points. The corresponding correlation and regression coefficients for the TraPPE-EH predictions of T_b are 0.993 and 0.984, respectively. There is significantly more scatter when the TraPPE-EH predictions are compared to values listed in *Knovel Critical Tables*,⁸⁴ with correlation coefficients of 0.92 and 0.93 for T_c and ρ_c , respectively. Based on the transferable nature of the TraPPE force field and the rigorous simulation protocol, we conclude that the TraPPE-EH predictions are more reliable than those in *Knovel Critical Tables* for compounds where experimental data are not available.

Comparison with the very limited experimental data for saturated liquid densities at elevated temperatures and saturated vapor pressures beyond the normal boiling point is also very good, with ρ_{sat} and P_{sat} reproduced to within 1.5% and 15%, respectively. In addition, the TraPPE-EH force field was used to predict vapor–liquid equilibrium properties for isoindole, benzimidazole, indazole, purine, benzo[c]thiophene, and benzisoxazole, for which no data were found in the literature.

The transferability of the TraPPE-EH force field was also assessed through computation of the pressure–composition diagrams for the binary mixtures of benzene/benzonitrile, benzene/phenol, and naphthalene/methanol, and the results for these binary systems are highly satisfactory.

Analysis of the liquid structures for the neat compounds and the binary mixtures indicates a competition between spatial distributions that allow for optimal packing through parallel orientation of neighboring arene rings and spatial distributions that better satisfy specific dipole–dipole and H-bonding interactions. Significant microheterogeneity is observed for all three binary mixtures.

■ ASSOCIATED CONTENT

§ Supporting Information

Description of the angle-bending and dihedral potentials for the semiflexible molecules and tables with the numerical data for the vapor–liquid coexistence curves. Machine-readable file (jp307328x_si_003.txt) containing the molecular structures and partial charges for all compounds and zip directory (jp307328x_si_001.zip) containing the molecular structures in pdb and mol2 formats. Zip directory (jp307328x_si_002.zip) containing Xmgrace source files for Figures 1–4, 6, 8, 9, 11, 12, 14, and 16. This material is available free of charge via the Internet at <http://pubs.acs.org>.

■ AUTHOR INFORMATION

Corresponding Author

*E-mail: siepmann@umn.edu.

Notes

The authors declare no competing financial interest.

■ ACKNOWLEDGMENTS

We thank Sam Keasler for providing the torsional parameters for 1,2-dihydroxybenzene. Financial support from the National Science Foundation (CBET-0756641 and CBET-1159837) and a University of Minnesota Doctoral Dissertation Fellowship

(N.R.) are gratefully acknowledged. Part of computer resources were provided by the Minnesota Supercomputing Institute.

■ REFERENCES

- (1) Pozharskii, A. F.; Soldatenkov, A. T.; Katritzky, A. R. *Heterocycles in Life and Society*; Wiley: New York, 1997.
- (2) Alexandru, T. B.; Daniela, C. O.; Alan, R. K. *Chem. Rev.* **2004**, *104*, 2777–2812.
- (3) Hunter, C. A. *Chem. Soc. Rev.* **1994**, *23*, 101–109.
- (4) Hunter, C. A.; Sanders, J. K. M. *J. Am. Chem. Soc.* **1990**, *112*, 5525–5534.
- (5) Bisson, A. P.; Carver, F. J.; Hunter, C. A.; Waltho, J. P. *J. Am. Chem. Soc.* **1994**, *116*, 10292–10293.
- (6) Muller-Dethlefs, K.; Hobza, P. *Chem. Rev.* **2000**, *100*, 143–168.
- (7) Braga, D.; Grepioni, F.; Desiraju, G. R. *Chem. Rev.* **1998**, *98*, 1375–1406.
- (8) Thaimattam, R.; Sharma, C. V. K.; Clearfield, A.; Desiraju, G. R. *Cryst. Growth Des.* **2001**, *1*, 103–106.
- (9) Aitipamula, S.; Thallapally, P. K.; Thaimattam, R.; Jaskolski, M.; Desiraju, G. R. *Org. Lett.* **2002**, *4*, 921–924.
- (10) Desiraju, G. R.; Gopalakrishnan, B.; Jetti, R. K. R.; Nagaraju, A.; Raveendra, D.; Sarma, J. A. R. P.; Sobhia, M. E.; Thilagavathi, R. *J. Med. Chem.* **2002**, *45*, 4847–4857.
- (11) Hu, J.; Barbour, L. J.; Gokel, G. W. *J. Am. Chem. Soc.* **2002**, *124*, 10940–10941.
- (12) Harper, S.; Pacini, B.; Avolio, S.; DiFilippo, M.; Migliaccio, G.; Laufer, R.; DeFrancesco, R.; Rowley, M.; Narjes, F. *J. Med. Chem.* **2005**, *48*, 1314–1317.
- (13) Sun, W.-H.; Shao, C.; Chen, Y.; Hu, H.; Sheldon, R. A.; Wang, H.; Leng, X.; Jin, X. *Organometallics* **2002**, *21*, 4350–4355.
- (14) Felker, P. M.; Maxton, P. M.; Schaeffer, M. W. *Chem. Rev.* **1994**, *94*, 1787–1805.
- (15) Leopold, K. R.; Fraser, G. T.; Novick, S. E.; Klemperer, W. *Chem. Rev.* **1994**, *94*, 1807–1827.
- (16) Mueller-Dethlefs, K.; Dopfer, O.; Wright, T. G. *Chem. Rev.* **1994**, *94*, 1845–1871.
- (17) Hobza, P.; Selzle, H. L.; Schlag, E. W. *Chem. Rev.* **1994**, *94*, 1767–1785.
- (18) Chalasinski, G.; Szczesniak, M. M. *Chem. Rev.* **1994**, *94*, 1723–1765.
- (19) Sinnokrot, M. O.; Valeev, E. F.; Sherrill, C. D. *J. Am. Chem. Soc.* **2002**, *124*, 10887–10893.
- (20) Sinnokrot, M. O.; Sherrill, C. D. *J. Phys. Chem. A* **2004**, *108*, 10200–10207.
- (21) Tauer, T. P.; Sherrill, C. D. *J. Phys. Chem. A* **2005**, *109*, 10475–10478.
- (22) Sinnokrot, M. O.; Sherrill, C. D. *J. Phys. Chem. A* **2006**, *110*, 10656–10668.
- (23) Zhao, Y.; Truhlar, D. G. *J. Phys. Chem. A* **2005**, *109*, 4209–4212.
- (24) Reyes, A.; Tlenkopatchev, M. A.; Fomina, L.; Guadarrama, P.; Fomine, S. *J. Phys. Chem. A* **2003**, *107*, 7027–7031.
- (25) Ringer, A. L.; Figgs, M. S.; Sinnokrot, M. O.; Sherrill, C. D. *J. Phys. Chem. A* **2006**, *110*, 10822–10828.
- (26) van der Avoird, A.; Podeszwa, R.; Szalewicz, K.; Leforestier, C.; van Harreveld, R.; Bunker, P. R.; Schnell, M.; von Helden, G.; Meijer, G. *Phys. Chem. Chem. Phys.* **2010**, *12*, 8219–8240.
- (27) Cornell, W. D.; Cieplak, P.; Bayly, C. I.; Gould, I. R.; aand, K. M.; Merz, J.; Ferguson, D. M.; Spellmeyer, D. C.; Fox, T.; Caldwell, J. W.; Kollman, P. A. *J. Am. Chem. Soc.* **1995**, *117*, 5179–5197.
- (28) Jorgensen, W. L.; McDonald, N. A. *J. Mol. Struct. (THEOCHEM)* **1998**, *424*, 145–155.
- (29) Jorgensen, W. L.; McDonald, N. A. *J. Phys. Chem. B* **1998**, *102*, 8049–8059.
- (30) Feller, S. E.; MacKerell, A. D., Jr. *J. Phys. Chem. B* **2000**, *104*, 7510–7515.
- (31) Lopes, P. E. M.; Lamoureux, G.; Mackerell, A. D. *J. Phys. Chem. B* **2007**, *111*, 2873–2885.
- (32) Lopes, P. E. M.; Lamoureux, G.; Mackerell, A. D. *J. Comput. Chem.* **2009**, *30*, 1821–1838.

- (33) Oosterbrink, C.; Villa, A.; Mark, A. E.; van Gunsteren, W. F. *J. Comput. Chem.* **2004**, *25*, 1656–1676.
- (34) Christen, M.; Hunenberger, P. H.; Bakowies, D.; Baron, R.; Burgi, R.; Geerke, D. P.; Heinz, T. N.; Kastenholz, M. A.; Krautler, V.; Oosterbrink, C.; Peter, C.; Trzesniak, D.; van Gunsteren, W. F. *J. Comput. Chem.* **2005**, *26*, 1719–1751.
- (35) Contreras-Camacho, R. O.; Ungerer, P.; Boutin, A.; Mackie, A. D. *J. Phys. Chem. B* **2004**, *108*, 14109–14114.
- (36) Contreras-Camacho, R. O.; Ungerer, P.; Ahunbay, M. G.; Lachet, V.; Perez-Pellitero, J.; Mackie, A. D. *J. Phys. Chem. B* **2004**, *108*, 14114–14123.
- (37) Ahunbay, M. G.; Perez-Pellitero, J.; Contreras-Camacho, R. O.; Teuler, J.-M.; Ungerer, P.; Mackie, A. D.; Lachet, V. *J. Phys. Chem. B* **2005**, *109*, 2970–2976.
- (38) Bonnaud, P.; Nieto-Draghi, C.; Ungerer, P. *J. Phys. Chem. B* **2007**, *111*, 3730–3741.
- (39) Nieto-Draghi, C.; Bonnaud, P.; Ungerer, P. *J. Phys. Chem. C* **2007**, *111*, 15686–15699.
- (40) Nieto-Draghi, C.; Bonnaud, P.; Ungerer, P. *J. Phys. Chem. C* **2007**, *111*, 15942–15951.
- (41) Perez-Pellitero, J.; Ungerer, P.; Mackie, A. D. *J. Phys. Chem. B* **2007**, *111*, 4460–4466.
- (42) Potoff, J. J.; Siepmann, J. I. *AIChE J.* **2001**, *47*, 1676–1682.
- (43) Rai, N.; Siepmann, J. I. *J. Phys. Chem. B* **2007**, *111*, 10790–10799.
- (44) Martin, M. G.; Siepmann, J. I. *J. Phys. Chem. B* **1998**, *102*, 2569–2577.
- (45) Martin, M. G.; Siepmann, J. I. *J. Phys. Chem. B* **1999**, *103*, 4508–4517.
- (46) Chen, B.; Siepmann, J. I. *J. Phys. Chem. B* **1999**, *103*, 5370–5379.
- (47) Wick, C. D.; Martin, M. G.; Siepmann, J. I. *J. Phys. Chem. B* **2000**, *104*, 8008–8016.
- (48) Maerzke, K. A.; Schultz, N. E.; Ross, R. B.; Siepmann, J. I. *J. Phys. Chem. B* **2009**, *113*, 6415–6425.
- (49) Chen, B.; Potoff, J. J.; Siepmann, J. I. *J. Phys. Chem. B* **2001**, *105*, 3093–3104.
- (50) Stubbs, J. M.; Potoff, J. J.; Siepmann, J. I. *J. Phys. Chem. B* **2004**, *108*, 17596–17605.
- (51) Wick, C. D.; Stubbs, J. M.; Rai, N.; Siepmann, J. I. *J. Phys. Chem. B* **2005**, *109*, 18974–18982.
- (52) Lubna, N.; Kamath, G.; Potoff, J. J.; Rai, N.; Siepmann, J. I. *J. Phys. Chem. B* **2005**, *109*, 24100–24107.
- (53) Wick, C. D.; Martin, M. G.; Siepmann, J. I.; Schure, M. R. *Int. J. Thermophys.* **2001**, *22*, 111–120.
- (54) Sokkalingam, N.; Kamath, G.; Coscione, M.; Potoff, J. J. *J. Phys. Chem. B* **2009**, *113*, 10292–10297.
- (55) Chen, B.; Xing, J.; Siepmann, J. I. *J. Phys. Chem. B* **2000**, *104*, 2391–2401.
- (56) Ketko, M. H.; Rafferty, J. J.; Siepmann, J. I.; Potoff, J. J. *Fluid Phase Equilib.* **2008**, *274*, 44–49.
- (57) Zhang, L.; Siepmann, J. I. *Collect. Czech. Chem. Commun.* **2010**, *75*, 577–591.
- (58) Schroer, J. W.; Monson, P. A. *J. Chem. Phys.* **2001**, *114*, 8950.
- (59) Zhao, X. S.; Chen, B.; Karaborni, S.; Siepmann, J. I. *J. Phys. Chem. B* **2005**, *109*, 5368–5374.
- (60) Rai, N.; Bhatt, D.; Siepmann, J. I.; Fried, L. E. *J. Chem. Phys.* **2008**, *129*, 194510.
- (61) Lorentz, H. A. *Ann. Phys.* **1881**, *12*, 127.
- (62) Berthelot, D. C. R. *Hebd. Seanc. Acad. Sci. Paris* **1898**, *126*, 1703.
- (63) Maitland, G. C.; Rigby, M.; Smith, E. B.; Wakeham, W. A. *Intermolecular Forces: Their Origin and Determination*; Pergamon Press: Oxford, U.K., 1987.
- (64) Harismiadis, V. I.; Panagiotopoulos, A. Z.; Tassios, D. P. *Fluid Phase Equilib.* **1994**, *94*, 1.
- (65) Halgren, T. A. *J. Comput. Chem.* **1996**, *17*, 490.
- (66) Delhomelle, J.; Millie, P. *Mol. Phys.* **2001**, *99*, 619.
- (67) Becke, A. D. *J. Chem. Phys.* **1993**, *98*, 5648–5652.
- (68) Perdew, J. P. *Phys. Rev. B* **1986**, *33*, 8822–8824.
- (69) Krishnan, R.; Binkley, J. S.; Seeger, R.; Pople, J. A. *J. Chem. Phys.* **1980**, *72*, 650–654.
- (70) Zhao, X. S. Ph.D. Dissertation, University of Minnesota, Minneapolis, MN, 2008.
- (71) Kelly, C. P.; Cramer, C. J.; Truhlar, D. G. *J. Theor. Comput. Chem.* **2005**, *1*, 1133–1152.
- (72) Chamberlin, A. C.; Kelly, C. P.; Thompson, J. D.; Xidos, J. D.; Li, J.; Hawkins, G. D.; Winget, P. D.; Zhu, T.; Rinaldi, D.; Liotard, D. A.; Cramer, C. J.; Truhlar, D. G.; Frisch, M. J. *MN-GSM*, version 6.0; University of Minnesota, Minneapolis, MN, 2006.
- (73) Panagiotopoulos, A. Z. *Mol. Phys.* **1987**, *61*, 813–826.
- (74) Panagiotopoulos, A. Z.; Quirke, N.; Stapleton, M.; Tildesley, D. *J. Mol. Phys.* **1988**, *63*, 527–545.
- (75) Allen, M. P.; Tildesley, D. J. *Computer Simulation of Liquids*; Clarendon Press: Oxford, U.K., 1987.
- (76) Frenkel, D.; Smit, B. *Understanding Molecular Simulation: From Algorithms to Applications*; Academic Press: San Diego, 1996.
- (77) Siepmann, J. I.; Frenkel, D. *Mol. Phys.* **1992**, *75*, 59–70.
- (78) Vlugt, T. J. H.; Martin, M. G.; Smit, B.; Siepmann, J. I.; Krishna, R. *Mol. Phys.* **1998**, *94*, 727–733.
- (79) Smit, B.; de Smedt, P.; Frenkel, D. *Mol. Phys.* **1989**, *68*, 931–950.
- (80) Rowlinson, J. S.; Widom, B. *Molecular Theory of Capillarity*; Oxford University Press: New York, 1989.
- (81) Rowlinson, J. S.; Swinton, F. L. *Liquids and Liquid Mixtures*; Butterworth: London, 1982.
- (82) Jorgensen, W. L.; Laird, E. R.; Ngyuen, T. B.; Tirado-Rives, J. *J. Comput. Chem.* **1993**, *14*, 206–215.
- (83) Jorgensen, W. L.; Maxwell, D. S.; Tirado-Rives, J. *J. Am. Chem. Soc.* **1996**, *118*, 11225–11236.
- (84) Knovel Critical Tables, 2nd ed.; Knovel: New York, 2003.
- (85) Lemmon, E.W.; McLinden, M.O.; Friend, D.G. *Thermophysical Properties of Fluid Systems*; NIST Chemistry WebBook; NIST Standard Reference Database Number 69; Linstrom, P.J., Mallard, W.G., Eds.; National Institute of Standards and Technology: Gaithersburg, MD, 2007; available at <http://webbook.nist.gov> (accessed March 2010).
- (86) Mooney, D. A.; Muller-Plathe, F.; Kremer, K. *Chem. Phys. Lett.* **1998**, *294*, 135–142.
- (87) Ferrando, N.; Lachet, V.; Teuler, J.-M.; Boutin, A. *J. Phys. Chem. B* **2009**, *113*, 5985–5995.
- (88) Design Institute for Physical Property Database (DIPPR); AIChE: New York, 1987.
- (89) BYU DIPPR 8001, *Thermodynamic Properties Database*; Brigham Young University: Provo, UT, 2005.
- (90) Stubbs, J. M.; Siepmann, J. I. *J. Am. Chem. Soc.* **2005**, *127*, 4722–4729.
- (91) Rai, N.; Rafferty, J. L.; Maiti, A.; Siepmann, J. I. *Fluid Phase Equilib.* **2007**, *260*, 199–211.
- (92) van Bolhuis, F.; Kiers, C. T. *Acta Crystallogr. B* **1978**, *34*, 1015–1016.
- (93) Horstmann, S.; Gardeler, H.; Bolts, R.; Gmehling, J. *J. Chem. Eng. Data* **1999**, *44*, 539–543.
- (94) Gmehling, J. *J. Chem. Eng. Data* **1982**, *27*, 371–373.
- (95) Thies, M. C.; Paulaitis, M. E. *J. Chem. Eng. Data* **1986**, *31*, 23–25.
- (96) Perry, R. H., Green, D. W., Eds. *Perry's Chemical Engineers' Handbook*, 7th ed.; McGraw-Hill, 1997; Chapter 2.
- (97) Hales, J. L.; Townsend, R. *J. Chem. Thermodyn.* **1972**, *4*, 763–772.
- (98) Chirico, R. D.; Knipmeyer, S. E.; Nguyen, A.; Steele, W. V. *J. Chem. Thermodyn.* **1993**, *25*, 1461–1494.
- (99) Das, A.; Frenkel, M.; Gadalia, N. A. M.; Kudchadker, S.; Marsh, K. N.; Rodgers, A. S.; Wilhoit, R. C. *J. Phys. Chem. Ref. Data* **1993**, *22*, 659–782.